Massive clumps in W43-main: Structure formation in an extensively shocked molecular cloud

F. Wyrowski, H. Liu, O. Sipilä, A. Izquierdo, T. Csengeri, A. Ginsburg, S. Spezzano, S. Leurini, P. Caselli, K. Menten

A&A, 685, A101 (2024)
https://doi.org/10.1051/0004-6361/202348959

Astronomy & Astrophysics

Massive clumps in W43-main: Structure formation in an extensively shocked molecular cloud

Y. Lin[1,2], F. Wyrowski[2], H. B. Liu[3], Y. Gong[2], O. Sipilä[1], A. Izquierdo[4,5], T. Csengeri[6], A. Ginsburg[7], G. X. Li[8], S. Spezzano[1], J. E. Pineda[1], S. Leurini[9], P. Caselli[1], and K. M. Menten[2]

[1] Max-Planck-Institut für Extraterrestrische Physik, Giessenbachstr. 1, 85748 Garching bei München, Germany
e-mail: ylin@mpe.mpg.de
[2] Max Planck Institute for Radio Astronomy, Auf dem Hügel 69, 53121 Bonn, Germany
[3] Department of Physics, National Sun Yat-Sen University, No. 70, Lien-Hai Road, Kaohsiung City 80424, Taiwan, ROC
[4] European Southern Observatory, Karl-Schwarzschild-Str. 2, 85748 Garching bei München, Germany
[5] Leiden Observatory, Leiden University, PO Box 9513, 2300 RA Leiden, The Netherlands
[6] OASU/LAB-UMR5804, CNRS, Université Bordeaux, allée Geoffroy Saint-Hilaire, 33615 Pessac, France
[7] Department of Astronomy, University of Florida, PO Box 112055, USA
[8] South-Western Institute for Astronomy Research, Yunnan University, Chenggong District, Kunming 650091, PR China
[9] INAF – Osservatorio Astronomico di Cagliari, Via della Scienza 5, 09047 Selargius (CA), Italy

Received 14 December 2023 / Accepted 30 January 2024

ABSTRACT

Aims. W43-main is a massive molecular complex undergoing starburst activities, located at the interaction of the Scutum arm and the Galactic bar. We aim to investigate the gas dynamics, in particular, the prevailing shock signatures from cloud to clump scales. We also look to assess the impact of shocks on the formation of dense gas and early-stage cores in OB cluster formation processes.
Methods. We carried out NOEMA and IRAM-30 m observations at 3 mm towards five molecular gas clumps in W43 main located within large-scale interacting gas components. We used CH_3CCH and H_2CS lines to trace the extended gas temperature and CH_3OH lines to probe the volume density of the dense gas components ($\gtrsim 10^5$ cm^{-3}). We adopted multiple tracers that are sensitive to different gas density regimes to reflect the global gas motions. The density enhancements constrained by CH_3OH and a population of NH_2D cores are correlated (in the spatial and velocity domains) with SiO emission, which is a prominent indicator of shock processing in molecular clouds.
Results. The emission of SiO (2–1) is extensive across the region (~4 pc) and it is contained within a low-velocity regime, hinting at a large-scale origin for the shocks. Position-velocity maps of multiple tracers show systematic spatio-kinematic offsets supporting the cloud-cloud collision-merging scenario. We identified an additional extended velocity component in the CCH emission, which coincides with one of the velocity components of the larger scale ^{13}CO (2–1) emission, likely representing an outer, less-dense gas layer in the cloud merging process. We find that the 'V-shaped', asymmetric SiO wings are tightly correlated with localised gas density enhancements, which is direct evidence of dense gas formation and accumulation in shocks. The dense gas that is formed in this way may facilitate the accretion of the embedded, massive pre-stellar and protostellar cores. We resolved two categories of NH_2D cores: those exhibiting only subsonic to transonic velocity dispersions and those with an additional supersonic velocity dispersion. The centroid velocities of the latter cores are correlated with the shock front seen via SiO. The kinematics of the ~0.1 pc NH_2D cores are heavily imprinted by shock activities and may represent a population of early-stage cores forming around the shock interface.

Key words. ISM: clouds – ISM: kinematics and dynamics – ISM: molecules – ISM: structure

1. Introduction

Massive stars profoundly influence the chemical and kinetic evolution of galaxies throughout their lifetimes via intense feedback effects, such as ionisation, stellar winds, and fierce death as exploding supernovae. However, our understanding of their formation process remains limited (Zinnecker & Yorke 2007; Motte et al. 2018). Compared to low-mass stars, OB stars originate from more massive and denser molecular environments, characterised by intense cloud-scale dynamics at $\gtrsim$1–10 pc (Vázquez-Semadeni et al. 2019; Padoan et al. 2020; Kumar et al. 2020). Understanding the formation and evolution of extreme star-forming clouds, which are in the high-mass end of the cloud mass spectrum and/or located in highly pressurised, turbulent environments, is of paramount importance for unravelling the origin of massive stars and clusters.

Supersonic shocks are common features associated with OB cluster forming molecular clouds, the origin of which can be stellar winds, expanding HII regions (Hill & Hollenbach 1978; Bertoldi 1989), cloud-cloud collisions (Fukui et al. 2021), or accretion and infall flows (e.g. Hennebelle & André 2013). In particular, cloud-cloud collision has been invoked as a possible mechanism of forming the dense, highly turbulent massive molecular clumps (for a recent review see Fukui et al. 2021). From a theoretical perspective, the shock-compressed gas layer is density-enhanced and prone to fragmentation (Whitworth et al. 1994b,a; Wu et al. 2017; Balfour et al. 2017), triggering the formation of gravitationally unstable cores and clumps at the collision interface (Habe & Ohta 1992; Anathpindika 2010; Takahira et al. 2014, 2018; Mocz & Burkhart 2018; Sakre et al. 2021; Cosentino et al. 2022). Shock compression can also cause convergent flows that further focus on the gas material towards

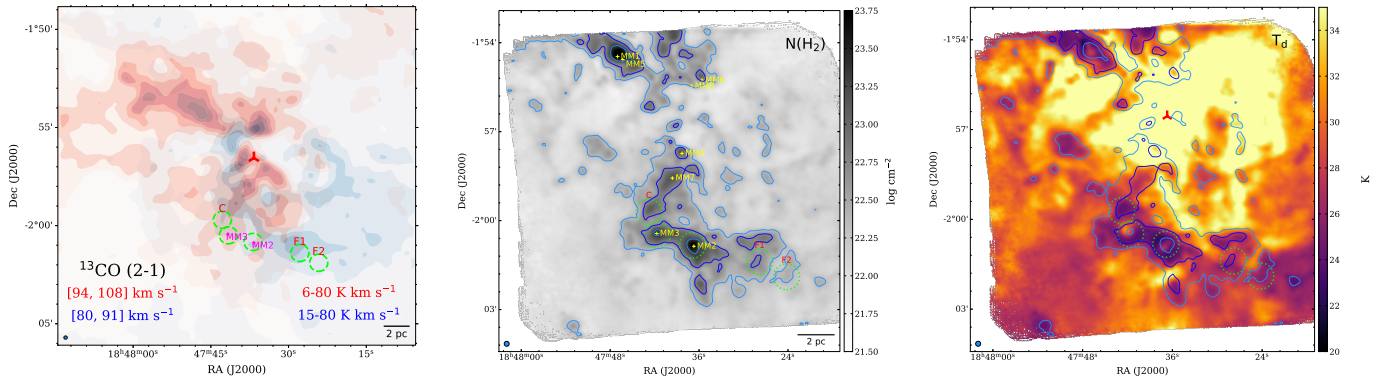

Fig. 1. Large-scale structure of W43-main and the distribution of the surveyed massive clumps. Left panel: target clumps overlaid on ^{13}CO (2–1) (obtained by IRAM 30m as in Carlhoff et al. 2013) integrated intensity maps (red and blue contours are integrated intensities over the respective velocity ranges shown in the figure). Middle and right panels: molecular hydrogen column density N(H_2) and dust temperature map T_d (>35 K temperatures are truncated for better contrast of the cold regions) of the W43-main molecular complex (10″ resolution, Lin et al. 2016). The three contour levels indicate column densities of 2.2×10^{22}, 5×10^{22}, and 2×10^{23} cm^{-3} (~1 g cm^{-2}), respectively. The pointed observations towards the 5 selected clumps are shown in green circles of primary beam size (FWHM) at 96 GHz. In the middle panel, the eight most massive clumps identified in Motte et al. (2003) are marked with yellow labels. Other target clumps are marked with red labels, following the names of C, F1 and F2. In the right panel, the red three-branched triangle marks the position of the W-R/OB cluster (Blum et al. 1999).

the forming cores and clumps therein (Inoue & Fukui 2013; Inoue et al. 2018). The collision velocity, initial density structures, and the kinematic state of the pre-collision clouds may be critical factors in setting the morphology, star formation efficiency (SFE) and protostellar mass distribution (Balfour et al. 2015, 2017; Liow & Dobbs 2020) of the compressed gas layer.

The W43 molecular cloud (of mass $M \sim 1\times10^6\ M_\odot$ and bolometric luminosity, $L_{\rm bol}\sim10^7\ L_\odot$, d~5.5 kpc) is among the most massive star-forming complexes in the Galaxy (Bally et al. 2010; Lin et al. 2016; Motte et al. 2022). It is a cloud hosting several star-burst clusters (Blum et al. 1999; Motte et al. 2003) and it may therefore be subject to ionisation-induced shocks ('radiation driven implosions', Bertoldi 1989; Bisbas et al. 2011). Located at the intersection of the (near end) Galactic bar and the Scutum arm at a distance of 5.49 kpc (Zhang et al. 2014), the cloud is enduring violent interactions of gas streams. There is wide-spread low-velocity ($\lesssim$20 km s^{-1}) SiO emission discovered toward W43, interpreted as signatures of shocks from large-scale colliding flows (Nguyen Luong et al. 2011). At even larger spatial scales, there are ~200 pc HI filaments showing velocity gradients feeding W43 (Motte et al. 2014), indicating that the turbulent convergent flows are continuous out to atomic gas. These facts suggest a highly dynamical process of OB cluster formation inside the cloud: W43 is an ideal site for understanding the impact of extensive shocks on the formation of OB clusters. oring massive star formation.

Molecular line and dust continuum surveys towards W43 at large scale (several tens of pc) reveal that there is a large amount of dense gas (Motte et al. 2003; Bally et al. 2010; Nguyen Luong et al. 2011; Carlhoff et al. 2013). The cloud is composed of two sub-clouds: W43-main and W43-south. W43-main is more massive and has a prominent 'Z'-shaped filamentary morphology (Motte et al. 2018). ^{13}CO (3–2) observations reveal two velocity components towards W43-main, 82 km s^{-1} and 94 km s^{-1}, intersecting at the southern ridge of the 'Z' cloud, which indicate cloud-cloud collisions (Kohno et al. 2021).

There are a number of massive star-forming clumps inside W43-main (Motte et al. 2003; Carlhoff et al. 2013, Lin et al. 2016); namely, clump MM2 and MM3 are the second and third most massive clumps in this cloud, after clump MM1, which all have masses of $\gtrsim$1000 $M_\odot$ and are actively forming stars (Motte et al. 2022; Cortes et al. 2019; Nony et al. 2023), representing potential OB cluster progenitors. In fact, considering the number of embedding clumps, among the seven OB cluster forming molecular clouds sampled in Lin et al. (2016), W43-main and W43-south have richer fragmentation than the other clouds, which may be a consequence of shock compression and subsequent self-gravitational fragmentation.

To investigate the cloud-clump connections of gas dynamics, the physical properties of the extended gas structures within massive clumps, of ~0.1 pc scale, are of primary interest. We conducted 3 mm wide-band observations with NOEMA and the IRAM 30m telescope towards five selected clumps located adjacently in the southern ridge of W43-main, where previous large-scale CO (2–1) observations have revealed extensive overlap of gas components of different velocities (Fig. 1, Carlhoff et al. 2013). These target clumps were identified from a 10″ hydrogen column density map of W43-main, derived by iterative spectral energy distribution (SED) fitting based on image combination technique utilising continuum from ground-based bolometers and space telescopes (Lin et al. 2016, Fig. 1). They span a wide mass range of 200–4000 $M_\odot$, while showing similar luminosity-to-mass ratios (~20, Table 1), indicative of similar evolutionary phase (Molinari et al. 2010) and may be formed coevally.

This paper is organised as follows. In Sect. 2, we describe the observations and data reduction procedure. In Sect. 3.1 we report the gas mass derived from 3 mm dust continuum and derive the dynamical timescale of the UCHII region in clump MM3. In Sect. 3.2, we constrain the temperature and density structure of the target clumps through several thermometers and CH_3OH lines. In Sect. 3.3, we present emission features of SiO and investigate their relation with dense gas formation. In Sect. 3.4, we reveal systematic velocity offsets of molecules tracing different gas densities. In Sects. 3.5 through Sect. 4, we describe the hyperfine fitting of CCH and NH_2D lines and report the discovery of a population of cold dense cores traced by compact NH_2D emission, along with an analysis of the chemical evolution of NH_2D with the aid of chemical models. In Sect. 5, we discuss the shock dynamics and put a special focus on the relation of the NH_2D cores with shocked gas and their multi-scale fragmentation properties.

Table 1. Properties of the five target clumps in W43-main.

Source	RA (J2000)	Dec (J2000)	Gas mass[(a)] ($10^2\ M_\odot$)	Luminosity[(a)] ($10^3\ L_\odot$)	L/M ($L_\odot/M_\odot$)	Category	$V_{\rm LSR}$[(b)] km s^{-1}
MM2	$18^h47^m36^s.86$	$-02°00'49''.8$	38	58	15	70 μm bright	91.3
MM3	$18^h47^m41^s.61$	$-02°00'29''.5$	19	51	26	UCHII	93.9
F1	$18^h47^m42^s.77$	$-01°59'42''.4$	3.0	6.6	22	IR dark	89.5
F2	$18^h47^m27^s.82$	$-02°01'23''.5$	2.3	43	19	IR dark	85.5
C	$18^h47^m42^s.77$	$-01°59'42''.4$	7.6	12	16	IR dark	91.7

Notes. [(a)] Gas mass and luminosity are calculated above column density thresholds $N_{\rm thres}$: for MM2, MM3 and C, $N_{\rm thres} = 5\times10^{22}$ cm^{-2}, for F1, $N_{\rm thres} = 4.5\times10^{22}$ cm^{-2}, for F2, $N_{\rm thres} = 2.2\times10^{22}$ cm^{-2}; the thresholds are chosen based on visual inspection of the $N(H_2)$ and bolometric luminosity maps (derived from integrating SED profile in a pixel-by-pixel basis) from Lin et al. (2016). [(b)]The system velocities ($V_{\rm LSR}$) are with reference to Urquhart et al. (2018) based on finding the identical or nearest clumps.

2. Observations and data reduction

The NOEMA pointed observations at 3 mm were taken between August to September 2019 with the D-array configuration in track-sharing mode (Project ID: S19AJ, PI: Y. Lin). Nine antennas were used during the observations, covering a baseline range of 32–176 m. On-source observations were conducted in 20–30 min intervals, interluded with observations on 1851+0035 as phase and amplitude calibrator. The bandpass calibrators are 3C273, 3C454.3, and 3C345, with the flux calibrator MWC349. The wide-band correlator PolyFix was used, which covers an instantaneous bandwidth of 31 GHz separated into eight subbands, with a fixed spectral resolution of 2 MHz (~6.2 km s^{-1} at 96 GHz). Multiple high-resolution spectral windows with 62.5 kHz (~0.2 km s^{-1}) channel spacing were placed to cover the molecular lines of interest. At a frequency of 96 GHz, the achieved angular resolution is 4.4″ and each pointing has a primary beam size (FWHM) of 53″.

We use the CLIC and MAPPING modules in the GILDAS software package[1] for calibration and imaging. The channels with line emission were identified by visual inspection with the IMAGER module and subtracted from the visibilities of low-resolution windows in the full frequency range to form the continuum. Similarly, to extract line emission, the continuum level was fitted and removed from each of the high-resolution backend chunks. We adopted natural weighting and cleaned the continuum and line cubes using the Hogbom algorithm (Högbom 1974).

As a short-spacing complement to add extended molecular line emission, IRAM 30m observations towards these clumps were taken during November 2019 to June 2020 with the EMIR receiver. A region of 1.7′ by 1.7′ was mapped around each source with the on-the-fly observing mode and then the five small datacubes were combined together to form a large datacube. Focus was checked on Saturn every 4 h and the pointing was determined every 1–1.5 h on 1749+096 or 1741-038. We followed the standard data reduction procedure with the CLASS module in GILDAS. The main beam efficiency ($\eta_{\rm mb}$[2]) was applied for conversion to main-beam temperatures ($T_{\rm mb}$).

We used the short-spacing data from the 30m telescope to generate pseudo-visibilities (task UVSHORT), which were added to the interferometry data. We image the three pointings of clump MM2, MM3, and C, and the two pointings of clump F1 and F2 together as two mosaic fields. We note that we do not utilise Nyquist sampling in the observations (e.g. as shown in Fig. 1), so the resultant mosaic fields have a spatially varying noise level. Joint imaging was then performed to obtain two set of combined spectral cubes; again, we adopted the Hogbom algorithm to obtain the clean images without providing any masks for the deconvolution process to search for the clean components; a plane-specific mask is usually not necessary when short-spacing information is available. In the final step, primary beam correction is applied. The synthesised beam of the final datacube is 4.7″ at 96 GHz and varies with frequency in the wide-band dataset. The achieved typical noise level (5σ) is ~0.05 K. The molecular lines of particular interest are listed in Table 2, which are all covered by the high-resolution chunks. For all these lines, we use the combined spectral cubes for the analysis.

Table 2. Line parameters for the 3 mm molecular lines used in the analysis.

Transition	Rest frequency (GHz)	$E_{\rm up}$ (K)	$n_{\rm crit}$ (cm^{-3})
HC_3N (9–8)	81.881	19.6	5.6×10^4
CS (2–1)	97.980	7.1	8.9×10^4
$H^{13}CO^+$ (1–0)	86.754	4.2	3.5×10^4
$CH_3OH\ 2_{-1,1}-1_{-1,0}\ E$	96.755	28.0	2.2×10^5
$CH_3CCH\ 5_0-4_0$	85.457	12.3	2.8×10^3
$CH_3CCH\ 6_3-5_3$	102.530	82.0	4.0×10^3
$CCH\ 1_{2,2}-0_{1,1}$	87.407	4.2	9.3×10^3
$SO\ 3_2-2_1$	99.299	9.2	4.3×10^4
SiO (2–1)	86.846	6.3	4.8×10^4
$H_2CS\ 3_{0,3}-2_{0,2}$	103.040	9.9	3.0×10^4
$H_2CS\ 3_{2,1}-2_{2,0}$	103.051	62.6	1.1×10^4
$NH_2D\ 1_{1,1}-1_{0,1}$	85.926	20.7	4.3×10^4

Notes. Line frequencies are taken from Cologne Database for Molecular Spectroscopy (CDMS) database (Endres et al. 2016). The critical density $n_{\rm crit}$ is calculated assuming a gas kinetic temperature of 30 K with no optical depth correction. The references of collisional rates for HC_3N is Faure et al. (2016), for SiO is Balança et al. (2018), for H_2CS is Wiesenfeld & Faure (2013), and for NH_2D Daniel et al. (2014).

3. Results

3.1. The 3 mm continuum

The 3 mm continuum maps of the five target clumps are shown in Fig. 2, overlaid on RGB maps of 8 μm (1.9″,

[1] http://www.iram.fr/IRAMFR/GILDAS/
[2] https://publicwiki.iram.es/Iram30mEfficiencies

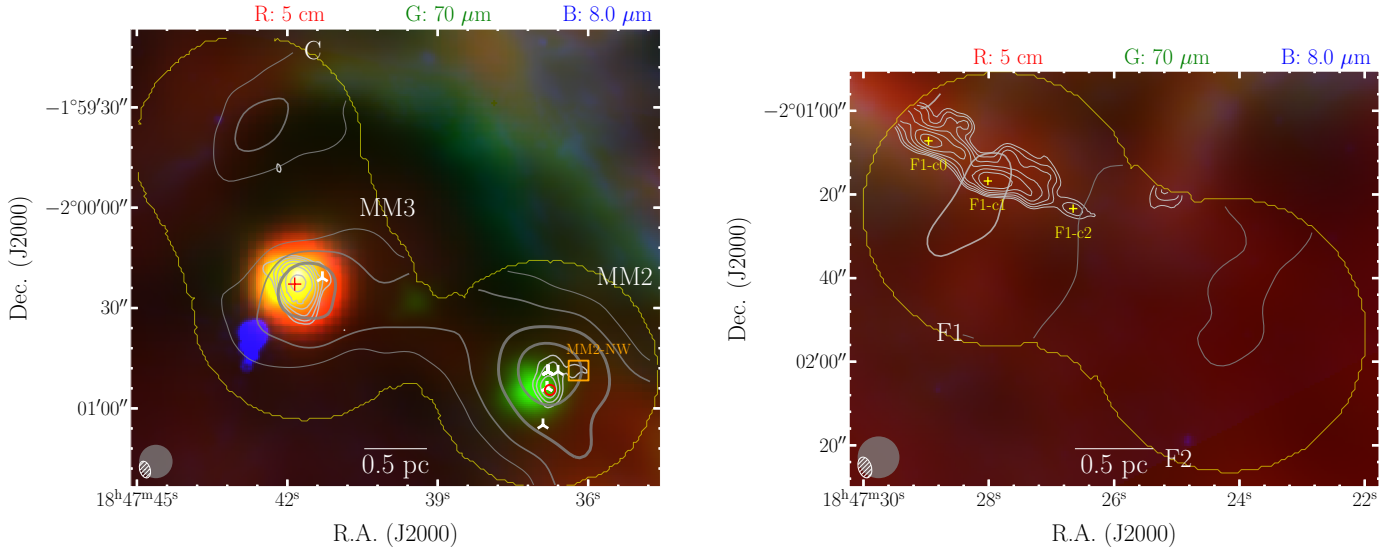

Fig. 2. Three-colour images of the clumps (red: GLOSTAR 5 cm radio continuum; green: *Herschel* Hi-GAL PACS 70 μm; blue: *Spitzer* 8.0 μm), overlaid with contour levels of NOEMA 3 mm continuum emission (white contours) and $N(H_2)$ (gray contours). The beams for the 3 mm continuum and the $N(H_2)$ map (10″) are shown in bottom left corner. The outer yellow solid lines indicate the NOEMA field-of-view of the observations. Left: target clump C, MM2, and MM3. The UCHII region (red cross) and OH maser (red circle), methanol masers (white three-branched triangles), and the northwestern substructure in clump MM2 (orange rectangle) are marked. Contour levels of the 3 mm continuum are logarithmic-spaced from $2\sigma_v$ (σ_v = 1.6 mJy beam^{-1}) to 225.0 mJy beam^{-1} with five intervals. Contour levels of the $N(H_2)$ map have values of $\log_{10}(N(H_2))$ = [22.75, 23.0, 23.25, 23.5] cm^{-2}. Right: target clump F1 and F2. Contour levels of 3 mm continuum are logarithmic-spaced from $2\sigma_v$ (σ_v = 0.4 mJy beam^{-1}) to 3.3 mJy beam^{-1} with five intervals. The three compact sources are marked with yellow pluses. Contour levels of the $N(H_2)$ map have values of $10^{[22.4,22.7]}$ cm^{-2}.

Carey et al. 2009), 70 μm (6″, Molinari et al. 2010), and 5 cm continuum (18″, GLOSTAR survey, Brunthaler et al. 2021). Clumps MM2 and MM3 are resolved with one dominant compact source in the center. These two sources are slightly elongated along the north-south direction. For clump MM2, there is an adjacent substructure to the northwest of the central compact source, marked as MM2-NW in the figure. The location of this substructure coincides well with a series of cores revealed by ALMA observations at 1.3 mm at 0.01-pc angular resolution (Cortes et al. 2019; Pouteau et al. 2023). For clump C and F2, there is no robust compact source detection towards the phase center. Clump F1 exhibits a filamentary structure of ∼0.2 pc in width, extending up to ∼1.2 pc in length. We marked the three compact sources along the filament of F1 as F1-c0, F1-c1, and F1-c2 (Fig. 2). However, these emission structures in F1 were not fully covered by our observations, truncating at the edge of the primary beam.

Clump MM3 is associated with an ultra-compact HII (UCHII) region, and it is the brightest UCHII in W43 (Bally et al. 2010). Assuming optically thin free-free emission with a spectral index of $\alpha = 0.1$, the intensity varies with frequency as $\nu^{-0.1}$. The free-free emission contribution to the 96 GHz band (3 mm) can be approximated by re-scaling the VLA X-band (8.46 GHz) continuum map[3] with $(96/8.46)^{-0.1}$. With preprocessing of the X-band image including convolution and regridding, the free-free contribution (integrated total flux, $S_{\rm int\,free-free}$ = 0.24 Jy) to the 3 mm continuum was subtracted in a pixel by pixel manner; the percentage of free-free emission to the total flux at 96 GHz is ∼34%.

The integrated fluxes at 3 mm, peak intensity and source size of the three clumps (MM2, MM3, and F1) estimated from 3 mm continuum are listed in Table 3. Assuming an average dust temperature of 30 K for MM2 and F1, and 100 K for MM3 (determined by the gas temperature in Sect. 3.2), and $\kappa_{100\,\rm GHz}$ = 0.245 cm^{-2} g^{-1}, with a gas-to-dust ratio of 100, we derived core masses from 3 mm continuum, which are listed in Table 3.

Additionally, we made an estimate on the dynamical age ($t_{\rm dyn}$) of the UCHII region embedded in clump MM3. We first estimated the number of Lyman continuum photons, $N_{\rm uv}$, with the equation (Mezger & Henderson 1967; Rubin 1968):

$$N_{\rm uv} = 7.5\times10^{46}\left(\frac{S_\nu}{\rm Jy}\right)\left(\frac{D}{\rm kpc}\right)\left(\frac{T_{\rm e}}{10^4\,\rm K}\right)^{-0.45}\left(\frac{\nu}{\rm GHz}\right)^{0.1}, \quad (1)$$

in which S_ν is the integrated flux, and D the distance, $T_{\rm e}$ the electron temperature, and ν the frequency. S_ν is obtained by summing up regions of flux densities >5 sigma with the VLA 8.46 GHz image, of ∼0.29 Jy. We assume $T_{\rm e}$ as a typical value of 7300 K (Tremblin et al. 2014) considering the galacto-centric distance of W43, which is 4.5 kpc (Zhang et al. 2014). The $N_{\rm uv}$ is calculated to be 6.6×10^{47} s^{-1}. The spectral type of the powering source based on $N_{\rm uv}$ is likely to be a O9.5-B0 ZAMs star (Panagia 1973).

With $N_{\rm uv}$, the dynamical timescale of the HII region, $t_{\rm dyn}$, can be computed following (Spitzer 1978; Dyson & Williams 1997),

$$t_{\rm dyn} = \left(\frac{4R_{\rm s}}{7c_{\rm s}}\right)\left[\left(\frac{R_{H\rm II}}{R_{\rm s}}\right)^{7/4} - 1\right], \quad (2)$$

where $c_{\rm s}$ is the isothermal sound speed in the ionised gas, ∼10–11 km s^{-1} (Bisbas et al. 2009). Here, $R_{\rm HII}$ is the radius of the HII region and $R_{\rm s}$ is the radius of the Strömgen sphere. Based on $\pi R^2_{\rm HII} = A$, where A is the >5 σ area from the 8.46 GHz image, $R_{\rm HII}$ is estimated to be 0.075 pc. $R_{\rm s}$ is calculated from

[3] Obtained from NRAO archive: http://www.aoc.nrao.edu/~vlbacald/ArchIndex.shtml

Table 3. Source properties from the 3 mm continuum emission.

Source	RA[(a)] (J2000)	Dec[(a)] (J2000)	$F^{(b)}_{\rm int}$ (Jy)	$I^{(b)}_{\rm peak}$ (mJy arcsec^{-2})	Size[(c)] ($''$)	$\sigma_{\rm v}$ (mJy beam^{-1})	Gas mass ($M_\odot$)
MM2	$18^{\rm h}47^{\rm m}36\overset{\rm s}{.}80$	$-02°00'54\overset{''}{.}0$	0.051	1.90	4.28	1.6	200
MM3[d]	$18^{\rm h}47^{\rm m}41\overset{\rm s}{.}79$	$-02°00'21\overset{''}{.}7$	0.463	7.40	7.75	1.6	900
F1	$18^{\rm h}47^{\rm m}27\overset{\rm s}{.}84$	$-02°01'17\overset{''}{.}0$	0.029	0.24	7.93	0.4	350

Notes. [(a)]The coordinates correspond to the position of the peak intensity. [(b)]The integrated intensity (above 5σ emission level) and peak intensity. [(c)]Radius, R, of the emission area A of $>5\sigma$, $A = \pi R^2$. [(d)]After subtraction of free-free emission.

Table 4. Information of lines used as thermometers.

Molecule	Transition	$E_{\rm up}$ (K)	C $T_{\rm mb}$ (K)	C ΔV (km s^{-1})	MM3 $T_{\rm mb}$ (K)	MM3 ΔV (km s^{-1})	MM2 $T_{\rm mb}$ (K)	MM2 ΔV (km s^{-1})	F1 $T_{\rm mb}$ (K)	F1 ΔV (km s^{-1})	F2 $T_{\rm mb}$ (K)	F2 ΔV (km s^{-1})
CH_3CCH	5(0)–4(0)	12.3	0.75	5.18, 2.36	1.80	1.88, 4.29	2.4	5.20	0.38	2.34, 1.9	0.20	3.5
	6(3)–5(3)	81.5	0.1		0.65		1.3		–		–	
H_2CS	3(1,3)–2(1,2)	22.9	0.65,0.62	3.41,3.20	3.0	2.33,5.19	5.50	4.20,11.70	0.20,0.12	2.18,5.69	0.10	2.0
	3(0,3)–2(0.2)[(a)]	9.89	0.60,0.40		1.78		3.80		0.15,0.08		0.08	
	3(2,2)–2(2,1)[(a)]	62.6										
	3(2,1)–2(2,0)	62.6	<0.05		0.20		1.0		<0.05		<0.05	
CH_2CHCN[(b)]	9(3,7)–8(3,6)	39.9					0.80	5.89				
	9(6,3)–8(6,2)	98.2					0.75					
	9(3,6)–8(3,5)	39.9					0.80					
	9(7,2)–8(7,1)	126.2					0.30					

Notes. The peak intensity ($T_{\rm mb}$) and corresponding line-width ($\Delta V = 2.355\sigma_{\rm v}$) are shown for each source. Whenever there are two velocity components, both line-widths are listed ,while the peak intensity is contributed from both components. For CH_3CCH only two representative transitions are shown whilst for both (5–4) and (6–5) line series all the k ladders are used in the fits, whenever robustly detected. [(a)]The two lines blend with each other. The listed line parameters are contributed from both lines. [(b)]Vinyl cyanide (CH_2CHCN) is only detected towards the center of clump MM2.

$R_{\rm s} = \left(\frac{3N_{\rm uv}}{4\pi n_0^2 \alpha_B}\right)^{1/3}$ in which $\alpha_{\rm B}$ is the radiative recombination coefficient; with T_e = 7300 K, $\alpha_{\rm B} = 3.3\times10^{-13}$ cm^3 s^{-1} (Spitzer 1978). For n_0, which represents initial gas density, we use a typical value of 10^5 cm^{-3} for UCHII region, which is close to the average gas density estimated from the 3 mm continuum (of $10^{5.5}$ cm^{-3}, using a gas mass of 900 $M_\odot$ and a radius of 0.20 pc with spherical assumption). Also, $t_{\rm dyn}$ is estimated to be ∼0.016 Myr, which is at the lower range of the typical lifetime for UC HII regions (of 0.01–0.1 Myr, Churchwell 2002; Mac Low et al. 2007).

3.2. Gas temperature and density distribution from LTE and non-LTE modelling

To characterise the physical properties of the dense gas inside the clumps, we first estimated the rotational temperature, $T_{\rm rot}$, and hydrogen volume density, $n(H_2)$. For this purpose, we adopt the CH_3CCH (6–5) and (5–4) ladders as thermometers and CH_3OH (2–1) A/E lines as densitometers.

CH_3CCH is widely distributed in lukewarm gas of relatively evolved massive star-forming clumps (Molinari et al. 2016a; Giannetti et al. 2017) and is an ideal tracer of the bulk gas structures (≳0.1–1 pc, Lin et al. 2022). Whenever detected, we also utilised H_2CS (3–2) and CH_2CHCN (9–8) lines which have multiple transitions to derive $T_{\rm rot}$. Compared to the emission of H_2CS and CH_3CCH lines, emission of CH_2CHCN lines is confined within 0.1 pc in the central region of MM2. The line parameters of these transitions and the properties of the observed lines at the position of peak emission of the five clumps are listed in Table 4.

Line series of CH_3OH have very different critical densities of different k components, hence, they compose an ideal densitometer of relatively high dynamical range, especially for the dense gas (≳10^5 cm^{-3}, Leurini et al. 2004, 2007; Lin et al. 2022).

3.2.1. Deriving the gas rotational temperature from thermometer lines

To estimate $T_{\rm rot}$ for the aforementioned thermometer lines, we utilise the XCLASS package (Möller et al. 2017) to establish single-component LTE models in a pixel by pixel manner. We keep the parameters of molecular column density, $N_{\rm mol}$, rotational temperature, $T_{\rm rot}$, and line-width ΔV, and centroid velocity, $V_{\rm LSR}$, as free parameters in the fitting (Figs. 3–4). We visually inspected the datacube first and find that there are subregions where more than one velocity component are present; therefore, we used an LTE model composed of two independent velocity components to describe the line emission. These subregions are identified by comparing the Akaike information criterion (AIC) of the one-component and two-component best-fit models. Such regions include the central regions of clumps MM3, C, and F1. After performing the fits,

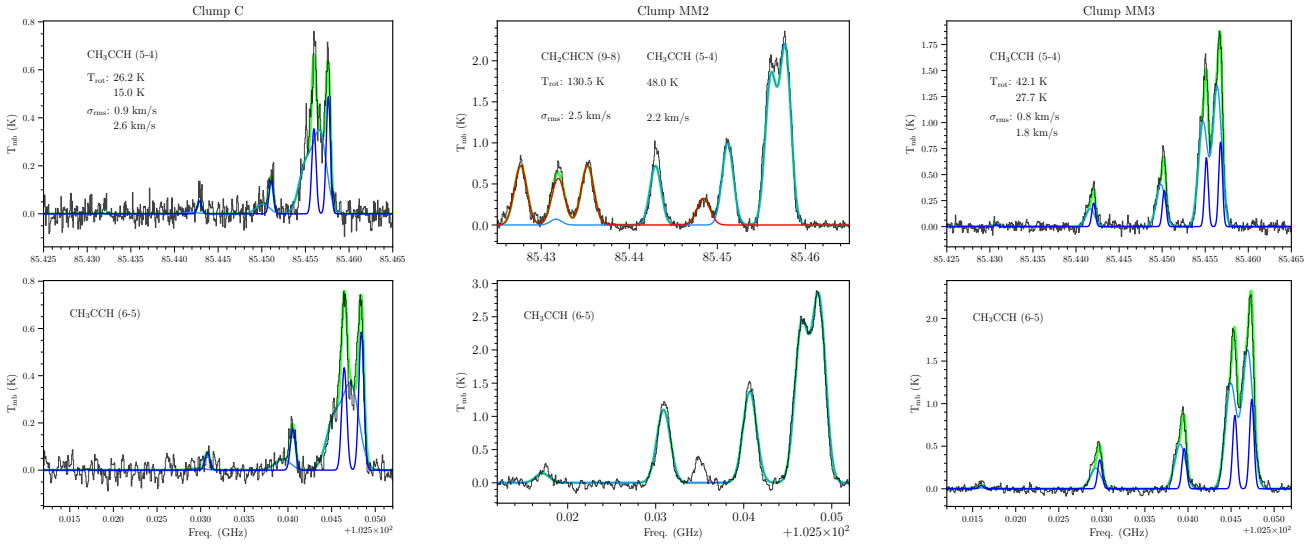

Fig. 3. CH_3CCH spectra at the peak emission of clumps C, MM2, and MM3. For clump MM2, the CH_2CHCN emission is detected, with red line showing the fitting result. In all plots, whenever there are more than one velocity component, both the composite line profile of the fits (green line) and the individual fit for each component (blue lines) are shown. The parameters of the peak intensity (T_{mb}) and linewidth (ΔV) are listed in Table 4.

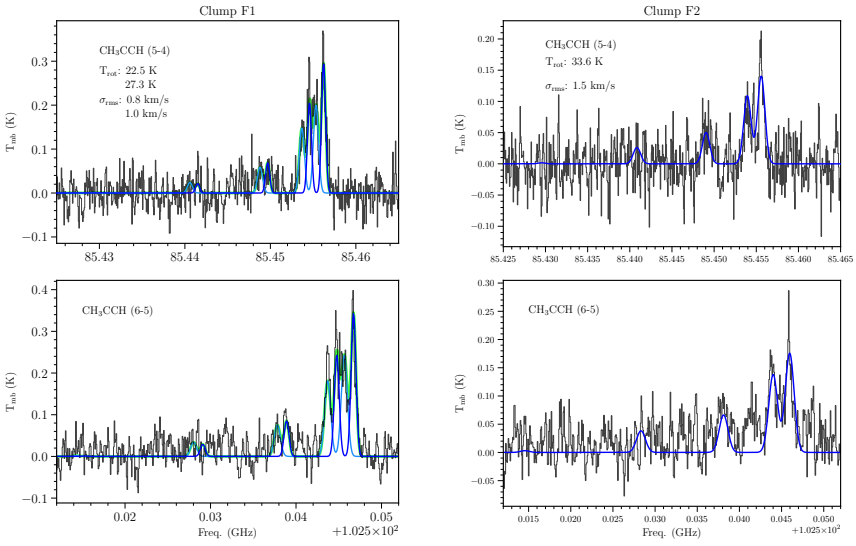

Fig. 4. Same as Fig. 3, but for clumps F1 and F2.

the set of two-component parameter maps were generated as follows. We examined the V_c map composed of only pixels where one-component model applies, with the pixels of two-component fits initially masked, and then calculate a weighted (by distance) centroid velocity from adjacent unmasked pixels to interpolate their masked neighboring pixels. The velocity values of these neighboring pixels are filled with the one of centroid velocities from the two-component model that is closer to the weighted velocity. The procedure is done progressively until all masked pixels with valid two-component fits are filled and produces two velocity component maps. The other parameter maps are generated correspondingly. The maps of the fitted T_{rot1} and T_{rot2} are shown in Fig. 5.

For clumps MM3 and C, we resolved a narrow velocity component of hotter gas and a broad velocity component of relatively cold gas (Fig. 3). Clump MM2 also exhibits two-component velocity features around the region of the most prominent emission. For clump F1, it seems there are more than two velocity components (Fig. 4); however, as it is limited by the achieved sensitivity (especially for the higher K ladder of these lines), a model of more than two velocity components cannot be robustly established.

The derived T_{rot} maps of CH_3CCH and H_2CS lines are shown in Figs. 5–6 and B.1. In general, the two T_{rot} distributions show similar features. Clump C has a relatively low temperature, mostly <25 K, with one gas component having temperature ∼10 K (right panel of Fig. 5). Clump MM3 has an overall warmer condition of 30–45 K, although it does not exhibit a strong peaking of gas temperature and the highest temperature seen by CH_3CCH is offset from the continuum peak. Clump MM2 has a significantly higher temperature in the central continuum peak, where the T_{rot} of CH_3CCH reaches ≳50 K and that of CH_2CHCN is up to ∼130 K. The difference between the two T_{rot} is expected as CH_3CCH emission is mostly coming from the extended gas of the colder envelope of the clumps (Molinari et al. 2016b; Giannetti et al. 2017; Lin et al. 2022). Clumps F1 and F2 show a rather uniform T_{rot} distribution, mostly below 25 K, comparable to that of clump C.

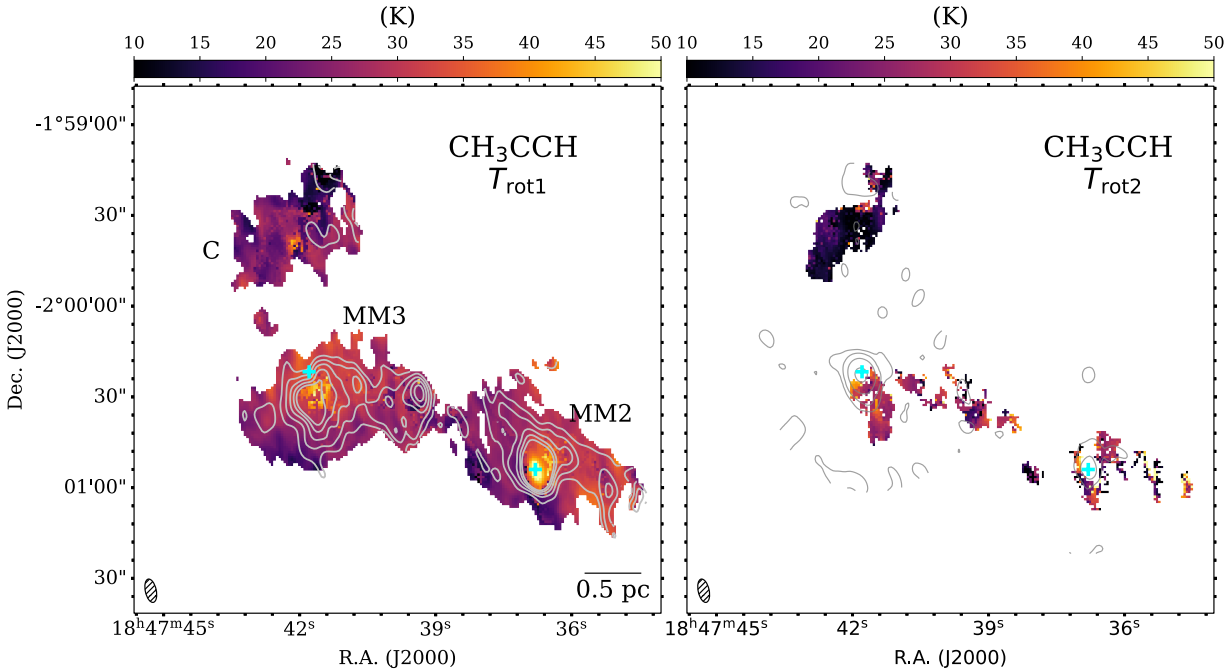

Fig. 5. Rotational temperature maps derived by CH_3CCH (6–5) and (5–4) lines. The left and right panel show the temperatures from the two-component LTE models separately. In the left panel, the contours represent integrated intensity map of CH_3CCH 5_2–4_2 line. The velocity range for integration is 80–100 km s^{-1}, and the contour levels are from 1.0 K km s^{-1} (5 σ) to 2 K km s^{-1} (0.3 times peak emission value of MM2) with five uniform intervals. In the right panel, the contours represent the 3 mm continuum emission and are logarithmically spaced from $2\sigma_v$ (σ_v = 1.6 mJy beam^{-1}) to 225.0 mJy beam^{-1} with five intervals (same as Fig. 2). In both plots, the cyan crosses indicate the position of the peak intensity of 3 mm emission.

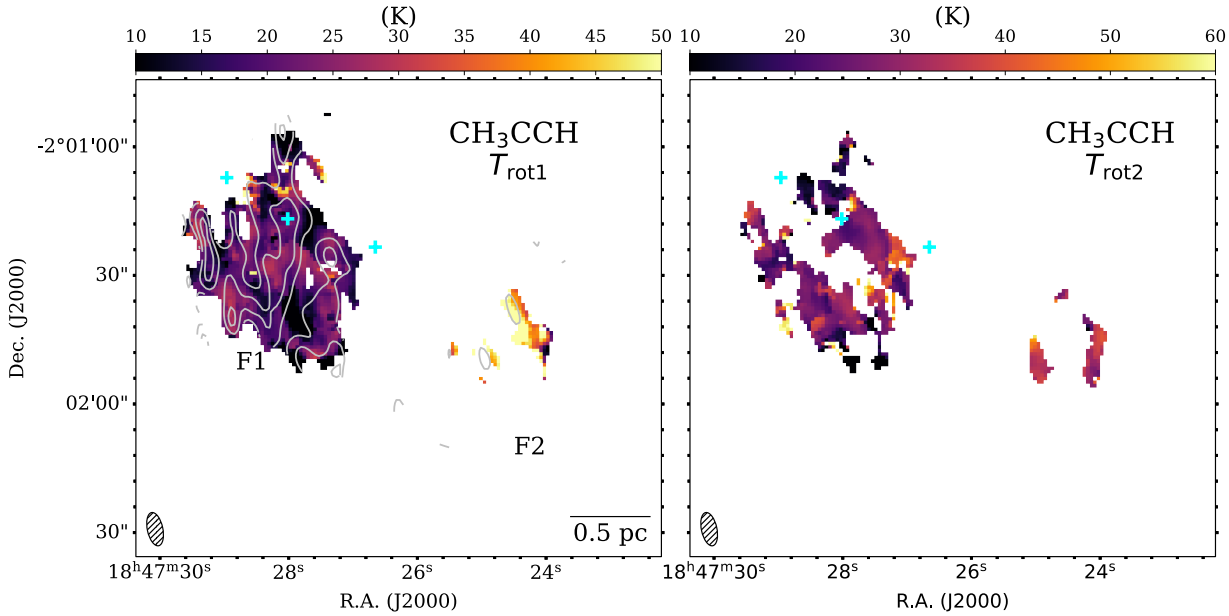

Fig. 6. Same as Fig. 5, but for the clumps F1 and F2. In the left panel the contours represent integrated intensity map of CH_3CCH 5_2-4_2 line. The velocity range for integration is 75–105 km s^{-1}, and the contour levels are from 0.45 K km s^{-1} (3σ) to 0.8 K km s^{-1} (0.9 times peak emission value of F1) with three uniform intervals. Cyan crosses mark the three cores from 3 mm continuum of F1 (as in Fig. 2, right panel).

3.2.2. Deriving the hydrogen gas density distribution from CH_3OH J = 2–1 A/E lines

To derive the hydrogen gas density, we first conducted one-component Gaussian fits of CH_3OH (2–1) A/E lines (for each K component) in a pixel-by-pixel manner and then used one-component non-LTE RADEX models (van der Tak et al. 2007) to predict the hydrogen volume density ($n(H_2)$) together with the methanol column density, N_{CH_3OH}, assuming an A-to-E ratio of 1, with T_{kin} assumed to (one-component) follow a normal distribution with mean value of T_{rot} derived from CH_3CCH lines (for available pixels) and a standard deviation of 10 K. In general, the intensity ratios of CH_3OH J-J-1 line series have a weak dependence on T_{kin}, so this assumption does not impact the derived parameters significantly, while indeed offering a better convergence.

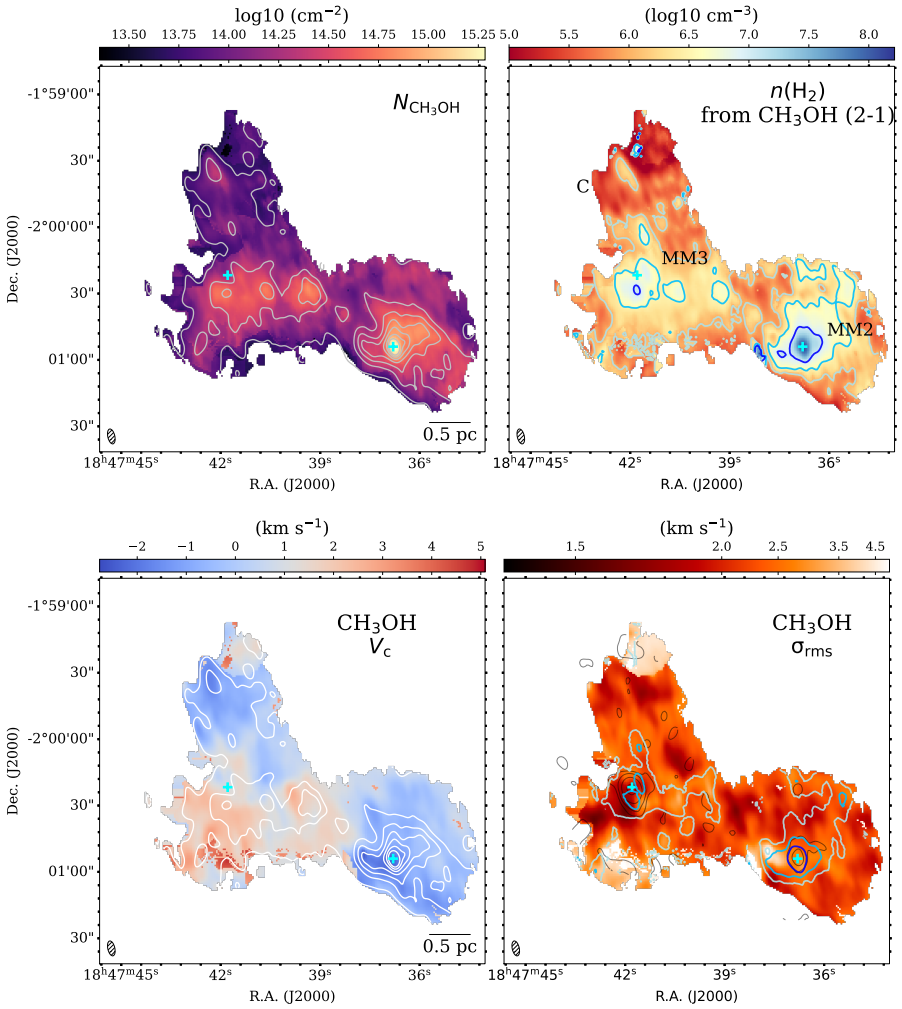

Fig. 7. Derived CH_3OH column density (E-type) and hydrogen volume density distribution from RADEX modelling for clumps MM2, MM3, and C (upper panel). One-component Gaussian fit result of CH_3OH (2–1) line series (lower panel). The centroid velocity (with respect to V_{LSR} = 91.7 km s^{-1}) and velocity dispersion ($\sigma_v = \Delta V/2.355$) distribution. In left panels, the contours represent integrated intensity levels of CH_3OH E-type 2(0, 1)–1(0, 1) line. The velocity range for integration is 85–100 km s^{-1}, and the contour levels are from 1.3 K km s^{-1} (7 σ) to 37 K km s^{-1} (0.75 times peak emission value of MM2) with seven uniform intervals. In right panels, the gray contours represent the 3 mm continuum emission, and are logarithmically spaced from 2σ_v (σ_v = 1.6 mJy beam^{-1}) to 225.0 mJy beam^{-1} with five intervals (same as Fig. 2). Cyan crosses mark the 3 mm continuum peak of MM2 and MM3. The green contours indicate n(H_2) levels of $10^{6.1}$ cm^{-3} and 10^7 cm^{-3}.

The CH_3OH (2–1) lines may also consist of more than one velocity component (Appendix A), but the confusion between different K ladders in this line series inhibits a robust multi-component Gaussian decomposition. Such an uncertain decomposition of line intensities will propagate to the RADEX modelling results and introduce a large bias in the estimating $n(H_2)$ and N_{CH_3OH}. We therefore retained a one-component Gaussian fit to describe the line profile of CH_3OH (2–1) lines.

We adopted a Markov chain Monte Carlo (MCMC) procedure with RADEX modelling, following the method described in Lin et al. (2022). The obtained maps of $n(H_2)$ and N_{CH_3OH} (A/E) from RADEX modelling and of the centroid velocity, V_c, and linewidth, σ_v, from the one-component Gaussian fit, are shown in Figs. 7 and 8 (right panel). The most prominent dense gas enhancement reside in clumps MM2 and MM3, with maximum gas densities reaching $\gtrsim 10^7$ cm^{-3}. In clump C, the gas densities also display increment around the peak emission but the density level ($10^{5.5}$–10^6 cm^{-3}) is close to the bulk gas density of MM2 and MM3. The central density enhancement of MM2 ($\sim 10^{7.5}$ cm^{-3}) coincides with its continuum peak and extends towards the west-east direction by an elongated structure of lesser density enhancement ($\sim 10^{6.5}$ cm^{-3}) showing a curved morphology. Cortes et al. (2019) resolved several cores in the northwest of the central cores in MM2 (more in Sect. 5.4), which lie close to the attaching region of the elongated structure and the central core. In clump MM3, the central density enhancement ($\sim 10^{6.5}$–10^7 cm^{-3}) is less concentrated. It peaks immediately to the south of the continuum peak. There are several smaller pockets of dense gas enhancement distributed in MM3 (smaller regions enclosed by green contours in Fig. 7), which are ~0.1–0.2 pc in size and remain mostly unresolved. In Sect. 3.3, we compare the distribution of the dense gas enhancement of clumps MM2 and MM3 with the velocity distribution (linewidths and velocity field) of the CH_3OH $2_{-1,1}$–$1_{-1,0}$, $5_{1,5}$-$4_{0,4}$ and SiO (2–1) lines.

The $n(H_2)$ distribution of clump F1 shows an enhancement at the CH_3OH emission peak near core F1-c1 and to the north,

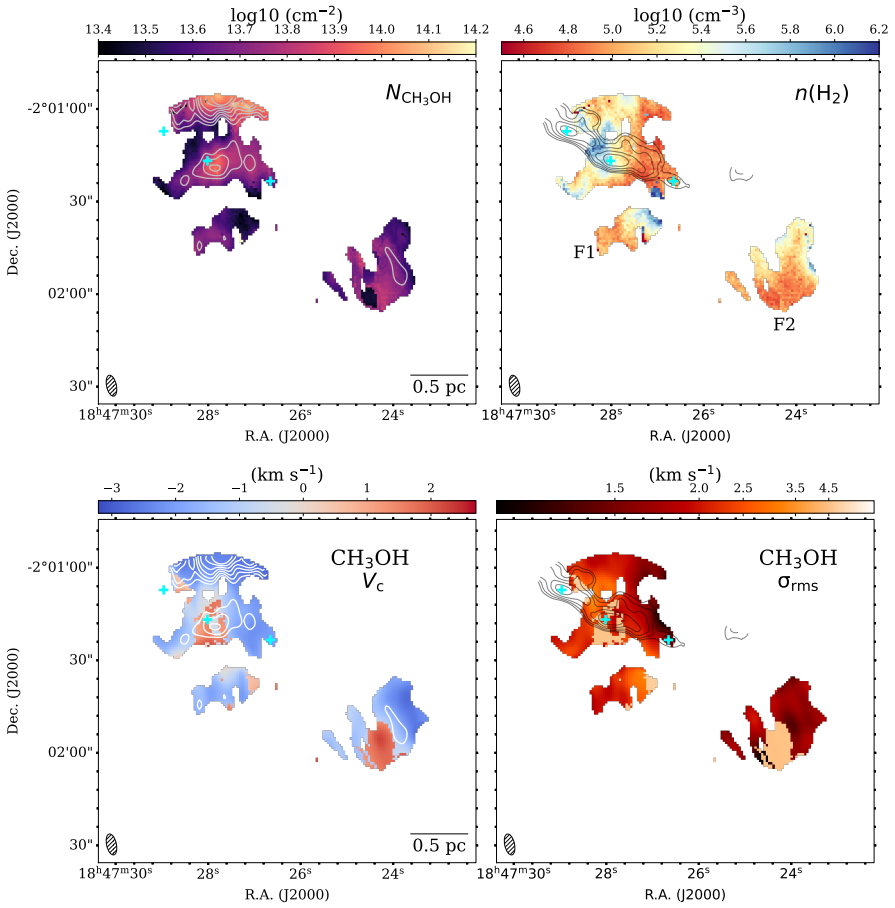

Fig. 8. Same as Fig. 7, but for the clumps F1 and F2. The centroid velocity is with respect to V_{LSR} = 85.5 km s^{-1} of clump F2. In the left panels, the contours represent integrated intensity levels of CH_3OH *E*-type 2(0, 1)-1(0, 1) line. The velocity range for integration is 80–95 km s^{-1}, and the contour levels are from 1.2 K km s^{-1} (7 σ) to 2.6 K km s^{-1} (0.75 times peak emission value of F1) with seven uniform intervals. Cyan crosses mark the three cores in 3 mm continuum of F1 (as in Fig. 2, right panel).

which is not fully covered by our observations. It also shows distributed density peaks at the edge of the extended CH_3OH emission. The maximum gas densities, however, reach only $\lesssim 10^6$ cm^{-3}. The F1-c1 core has an averaged gas density of $10^{5.5}$ cm^{-3}. Clump F2 shows a rather uniform distribution of gas densities, having values mostly below 10^5 cm^{-3}.

3.3. Characteristics of SiO emission and gas density enhancement

Commonly, SiO is used as a tracer of shock activities since relatively high-velocity shocks (shock velocity $\gtrsim$20 km s^{-1}) are needed to sputter SiO from dust grains in the gas phase (Schilke et al. 1997; Caselli et al. 1997; Jiménez-Serra et al. 2008) unless some SiO is trapped in the ice mantles. In the latter case, lower velocities may also allow for some of the SiO to go back to the gas phase via erosion (e.g. Jiménez-Serra et al. 2008); however, the abundance of SiO is much lower than in the case of faster shocks. To understand the shock activities and its induced gas dynamics at 0.1 pc scale, we analyzed the velocity features of the SiO (2–1) line and examined the spatial correlations between the excessive line wings and dense gas enhancement based on the $n(H_2)$ map (Fig. 7).

The distribution of the SiO emission (integrated intensity map, of the velocity range between 76.7–106.7 km s^{-1}) is shown in the left panel of Fig. 9. The two sub-regions showing the most intense SiO emission are located in the central region of clump MM2 and at the position of (35″, –10″) ($\Delta\alpha$, $\Delta\delta$) offset from MM2, respectively. The latter sub-region is located in the connection region of MM2 and MM3. The gas velocity field traced by SiO shows a pattern of complementary distribution: moving from clump C to MM3 and MM2 in the northeast to southwest direction, the velocity changes from being blue-shifted to red-shifted and again to blue-shifted (compared to the V_{LSR} of MM3). A similar picture is also revealed in the integrated intensity maps of the same velocity ranges of other lines shown in Fig. A.4. To further illustrate this pattern, we separated the blue-shifted and red-shifted velocity ranges and integrated the two velocity ranges individually, which are shown together in Fig. 9 (panel b). The two distributions of blue-shifted and red-shifted emission compose a 'Y-shaped' morphology. Particularly, the density enhancement of clump MM3 (shown as coloured contours in panel a) seems to follow the vertex region of the "Y" tightly, while the central region of clump MM2 lies in-between the two distributions.

In the lower panel of Fig. 9, the sub-regions showing a density enhancement of $>10^6$ cm^{-3} (indicated by contours in panel a of Fig. 9 based on the n(H_2) map) are shown together as shaded regions with the position-velocity (PV) diagrams following the three cuts (U, M, and L). The three position-velocity cuts are chosen to encompass the 'Y-shaped' structure of the SiO emission, to illustrate the emission associated along the ridge of most prominent density enhancements (linking central regions of

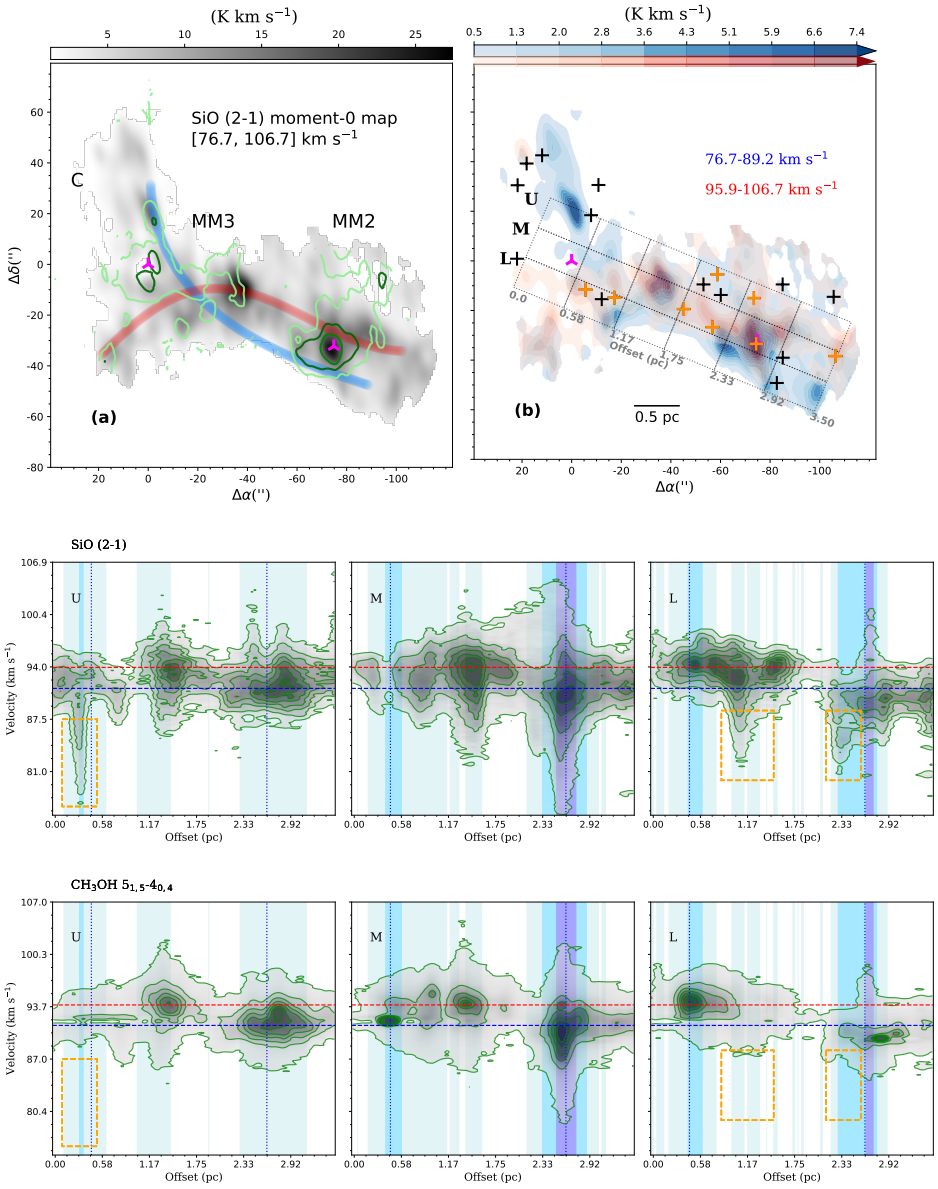

Fig. 9. SiO and dense gas distribution and position-velocity maps. Upper panel (a) Integrated intensity map of SiO (2–1) (76.7–106.7 km s^{-1}, gray scale) overlaid with the n(H$_2$) levels of 10^6, $10^{6.5}$, 10^7 cm^{-3} (in contours of various shades of green, respectively). The 3 mm continuum peaks of MM2 and MM3 are indicated as magenta crosses. The red and blue thick lines indicate the ridge of the emission of the blue-shifted and red-shifted SiO in panel b. (b) The integrated intensity maps (velocity ranges indicated in the plot) of the SiO (2–1) blue-shifted and red-shifted emission. The crosses in orange (with at least one broader velocity component of $\sigma_v > 0.85$ km s^{-1}, see Sect. 4) and black indicate the NH$_2$D cores. For plots a and b, RA and Dec offsets correspond to the relative position with respect to 3 mm continuum peak of MM3. Lower panel: position–velocity diagrams of SiO (2–1) (contour levels of 0.2–1.4 K km s^{-1} with six intervals) and CH$_3$OH 5$_{1,5}$-4$_{0,4}$ (contour levels of 0.1–10.3 K km s^{-1} with six intervals) line along the three cuts U, M, and L, as in the upper panel. The colour-shaded regions indicate the n(H$_2$) levels of 10^6, $10^{6.5}$, and 10^7 cm^{-3} (in light blue, blue, and purple). The V_{LSR} of MM2 and MM3 are indicated as red and blue horizontal lines (93.9 km^{-1} and 91.3 km^{-1}). Blue vertical dotted lines indicate the positions of the 3 mm continuum peak of MM2 and MM3.

MM3 and MM2) and the two offsets along the same direction. Each of the three cuts is averaged over a width of 0.35 pc as indicated in panel b of Fig. 9.

The PV diagrams are then extracted from the SiO (2–1) and CH$_3$OH 5$_{1,5}$–4$_{0,4}$ spectral cubes. The line wings of both emission mostly appear within 8 km/s around the V_{LSR} (low-velocity regime). Along the three cuts, SiO emission shows more extended line wings in both spatial and velocity regimes than that of CH$_3$OH 5$_{1,5}$–4$_{0,4}$. There is a broad red-shifted SiO velocity wing at offset 1.0–2.4 pc in the PV cut of M, which also extends to higher terminal velocities. The terminal velocities of SiO reach up to V_{LSR}±15 km s^{-1}, as seen from the U and M cuts. There are also several prominent wing components that appear asymmetric in the PV maps of SiO (indicated by orange rectangles in middle and lower panel of Fig. 9), with no counterparts in opposite velocity regime. These single, excessive line wings appear mostly blue-shifted and do not have counterparts in the CH$_3$OH emission; they are likely outcome of high-velocity shocks from outflow activities sputtering the cores of dust grains to release SiO (Snow & Witt 1996; Jiménez-Serra et al. 2008). It seems the density enhancement at the central region of clump MM2, at an offset of 1.8–3.2 pc (illustrated as blue and purple shaded regions around the blue dotted line), coincides with double-peaked velocity wings, while the density enhancement associated with the immediate vicinity of the continuum of MM3 is not associated with significant velocity wing features, as seen from the M cut of SiO PV map. The sub-regions of secondary density enhancement (indicated by light-blue shaded regions) are mostly correlated with prominent line wings.

For each PV cut, we separate the sampled area into six parts (panel b of Fig. 9) and plot the average spectra of SiO (2–1) and CH$_3$OH 5$_{1,5}$-4$_{0,4}$ lines in Fig. 10. We use a two-component Gaussian model to characterise the SiO (2–1) line profile. We obtained velocity dispersion of the narrow component (σ_n) ranging between 1.5–3.4 km s^{-1} with a mean value of ~1.7±1.5 km s^{-1}, and the σ_v of the broad component (σ_w) between 3.0–7.4 km s^{-1} with a mean value of ~4.6±1.5 km s^{-1}. We compare the broad-component subtracted narrow line profiles (in red) with the V_{LSR} of clumps MM2 and MM3 in Fig. 10. It can be seen that the majority of the peak velocities of the

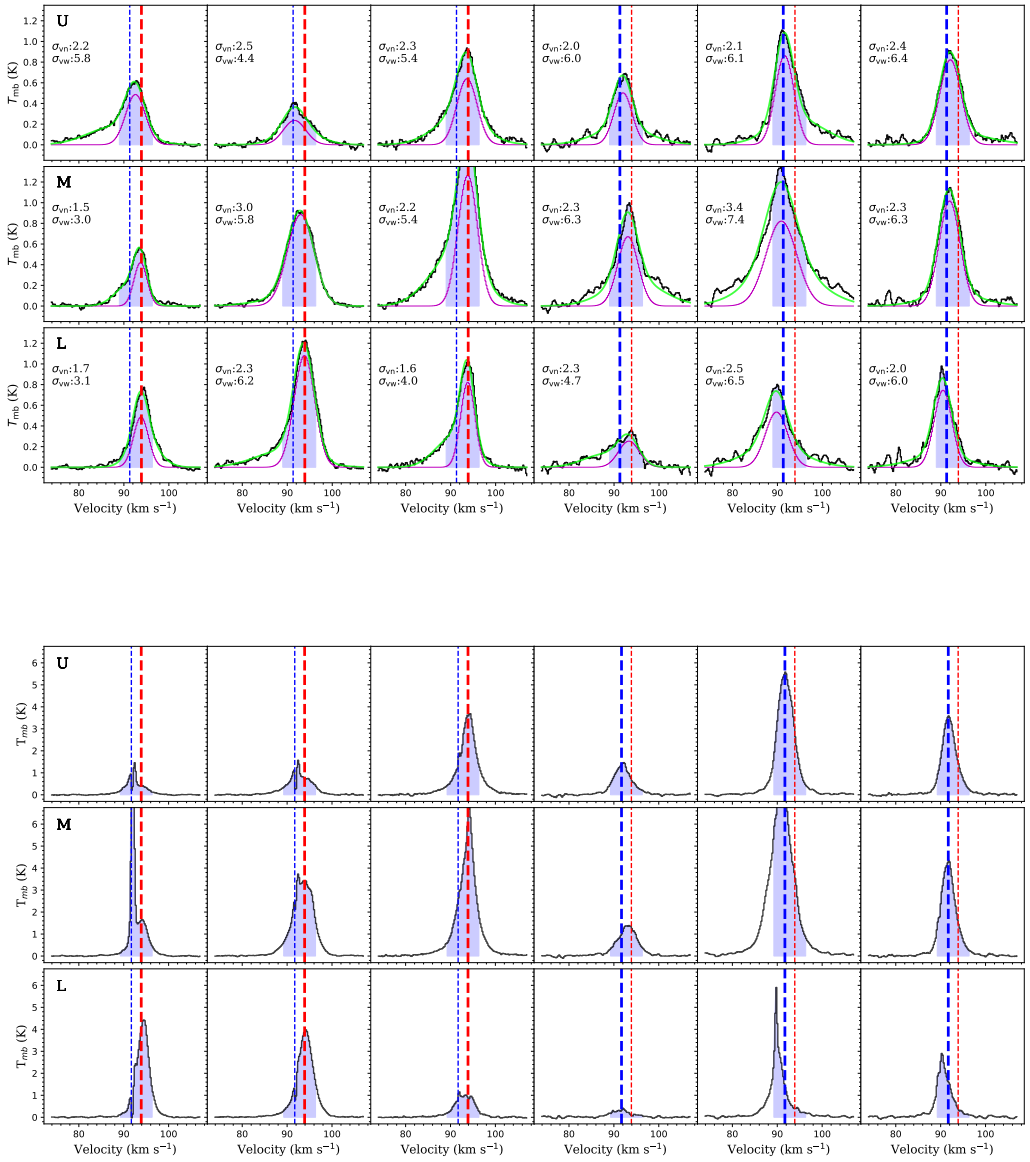

Fig. 10. Average spectra of SiO (2–1) (upper panel) and CH_3OH $5_{1,5}$–$4_{0,4}$ (lower panel) along the three PV cuts U, M, L as in panel b of Fig. 9. The spectra are arranged from northeast to southwest along the cuts. The blue and red dashed lines indicate the V_{LSR} of clump MM3 and MM2 (93.9 km s^{-1} and 91.3 km s^{-1}), with the thicker line corresponding to the V_{LSR} of either clump MM2 or MM3 at this position. The blue shaded regions indicate the line central velocity range from (91.3–2.5) km s^{-1} to (93.9+2.5) km s^{-1}, which is excluded from the integration of the intensity maps of panel b in Fig. 9. In the upper plot, the two-component Gaussian fit to the SiO line is shown additionally, as green line. The broad-component subtracted spectrum (narrow-component line profile) is shown as magenta line. The velocity dispersions for the two components are indicated in the figure, in unit of km s^{-1}.

narrow component are consistent with the peak velocity of the whole line profile and within the range of the V_{LSR} of MM2 and MM3.

3.4. Velocity distribution of different molecules: systematic velocity shift

In Figs. 11 and 12, we plot the PV diagrams along the three cuts U, M, and L in the northern region (Fig. 9) for molecular lines CCH $1_{1,0}$–$0_{1,1}$, HC_3N (9–8), $H^{13}CO^+$ (1–0), and SO 2_2–1_1, together with SiO (2–1) line. The emission of some of these transitions is similar to or even more extended than SiO.

In general the peak velocities of the CCH line coincide well with that of SiO along all three PV cuts, except the offset region at (0.8,2.4) pc in M cut, where peak velocities of CCH appear more blue-shifted. The peak velocities of the SO 2_2–1_1 line, on the other hand, show a slightly red-shifted tendency along the cuts. The velocity shift between both HC_3N and $H^{13}CO^+$ with respect to SiO is the most prominent and exist everywhere except the offset region of (1.3, 2.0) pc in the M and L cut. The peak velocities of HC_3N and $H^{13}CO^+$ appear in the more red-shifted regime, with the velocity shifts reaching up to ∼2 km s^{-1}.

From the PV maps of the CCH line, it is also clearly seen that at spatial offsets around clump MM2 in the L cut, there is a prominent red-shifted component which is not present in the SiO PV map. This component also exists in the HC_3N and $H^{13}CO^+$ PV map of cut L, but of a smaller spatial extension.

To further demonstrate this, we present the spectra of the CCH line along the three PV cuts in Fig. 13. The two velocity components are seen both in the main line of CCH $1_{1,0}$-$0_{1,1}$,

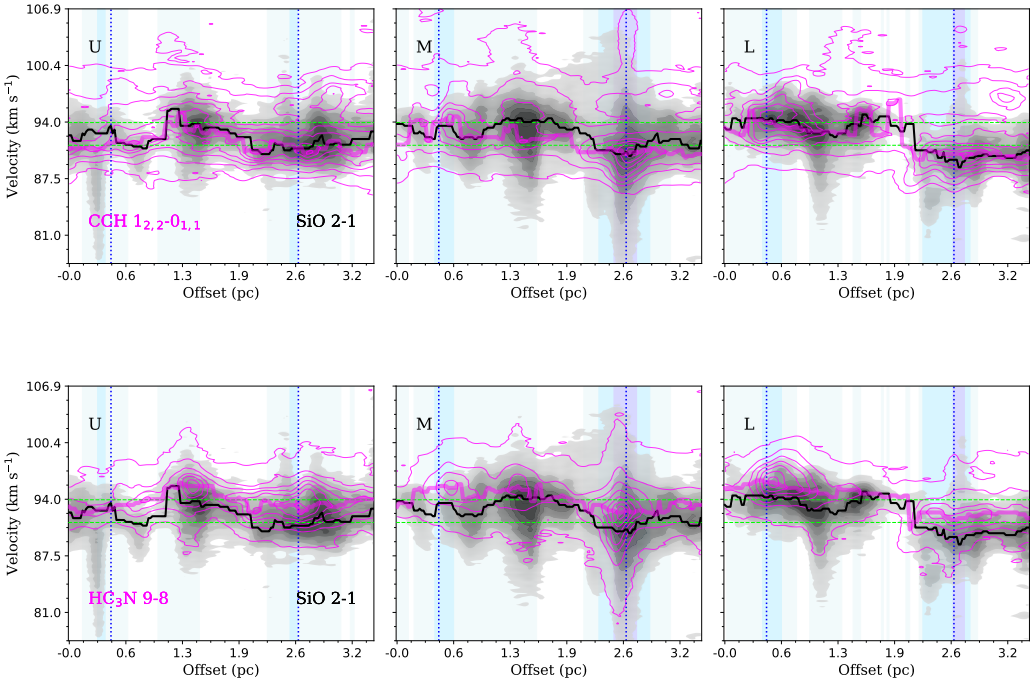

Fig. 11. Position-velocity diagram for CCH $1_{2,2}$–$0_{1,1}$, HC_3N (9–8) (in magenta contours) in comparison to that of SiO (2–1) (gray filled contours), along the U, M, and L cuts as illustrated in panel b of Fig. 9. The V_{LSR} of MM2 and MM3 are indicated as green horizontal lines (93.9 km^{-1} and 91.3 km^{-1}). The vertical dotted line and shaded regions follow those as in Fig. 9. The peak velocity along the spatial offset for SiO (2–1) and the respective molecular line (that have extended emission) in each plot are indicated as black and magenta lines.

which is slightly optically thick (τ_m~0.5–2.5 from hyperfine fitting, see Sect. 3.5) in this region, and the least intense satellite line CCH $1_{1,1}$-$0_{1,1}$ which is optically thin (τ<0.5, more in Sect. 4). This suggests that the two-component line profile is not an optical depth effect but produced by (at least) two velocity gas components. Also from the CCH PV maps, there are several prominent red-shifted wings at offset ~1.3 pc along U, M and L cut. These structures have terminal velocities reaching beyond V_{LSR}+10 km s^{-1}, and do not have clear counterparts in the PV maps of the other lines. We compared the velocity of the second component with the large-scale ^{13}CO (2–1) data obtained from the IRAM 30m legacy program HERO (Carlhoff et al. 2013) and found that it has a counterpart of similar velocity, confirming that this additional velocity component represents an outer, less dense gas layer in the cloud merging-collision process.

3.5. Hyperfine fitting of CCH lines

CCH (1–0) lines are split into hyperfine structures (*hfs*) that allow us to measure the excitation temperatures and optical depths. We conducted one-component and two-component fits and chose the best-fit model among them.

In Figs. C.1 and C.3, the fitted excitation temperature, T_{ex}, total CCH column density, N_{CCH}, and the centroid velocity and linewidth of CCH (1–0) lines towards clumps MM2, MM3, and C are shown. Figures C.2 and C.4 show the same maps towards clump F1 and F2. The emission of CCH is very extended especially in clumps MM2 and MM3. Clump C has CCH emission mostly in the north-west region. For clump MM3 in particular, the CCH emission around the UCHII regions has a sharp decrease of emission in the north-east direction, exhibiting an arc-like morphology. This is consistent with previous observations and predictions that CCH in active star-forming regions is efficiently converted to other molecules (e.g. Beuther et al. 2008; Jiang et al. 2015). The derived N_{CCH} ranges between $10^{15.5}$–$10^{16.5}$ cm^{-2}. The T_{ex} of CCH is mostly ~5–10 K, with local maxima reaching 25 K at the periphery of the central region of clump MM2 and at intersection region of MM2 and MM3. Comparing the velocity dispersion (σ_{v_1} and σ_{v_2}) to T_{ex}, we again resolve, similarly as CH_3CCH lines, that the regions of high T_{ex} in clumps MM2 and MM3 are displaying larger line-widths, while in clump C, T_{ex} and line-widths seem anti-correlated.

The velocity field of CCH in the regions where CH_3CCH is detected has a generally consistent distribution. There are prominent red-shifted components of CCH reaching +8 km s^{-1} in the intersection region of clumps MM2 and MM3, and in the southern part of MM2 (as illustrated also in Fig. 11). As discussed in Sect. 3.4, these red-shifted components peaking at 96–98 km s^{-1} may represent an outer layer of the clouds in collision.

4. NH_2D emission and NH_2D-traced cores

NH_2D 1(1,1)–1(0,1) line also exhibits hyperfine structures. Compared to CCH, emission of NH_2D 1(1,1)–1(0,1) is more localised and compact. The integrated intensity maps of NH_2D 1(1,1)–1(0,1) are shown in Fig. 14 (left panel) for the northern and southern regions, respectively. In comparison to the 3 mm dust continuum, we see that only clump MM2 and core F1-c1 has strong emission of NH_2D.

To better characterise the localised emission of the NH_2D line, we run the `dendrogram` (Rosolowsky et al. 2008) algorithm on NH_2D spectral cube to extract physical parameters that define these NH_2D-traced subregions. For the `dendrogram` input parameters, we set both `min_value` and `min_delta` to be 3σ of the noise level, and `min_npix` to be the number of pixels inside one beam, which means we consider structures of peak emission larger than 3σ and size larger than one beam and are at least 3σ more significant than the emission of their lower

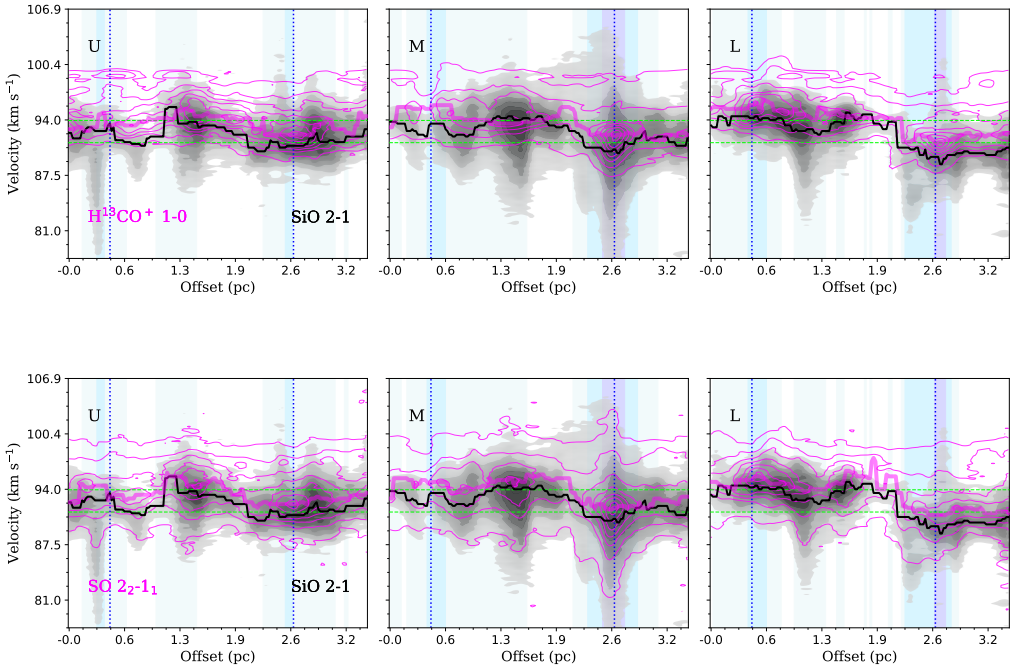

Fig. 12. Same as Fig. 11, but for $H^{13}CO^+$ (1–0) and SO 2_2–1_1 lines.

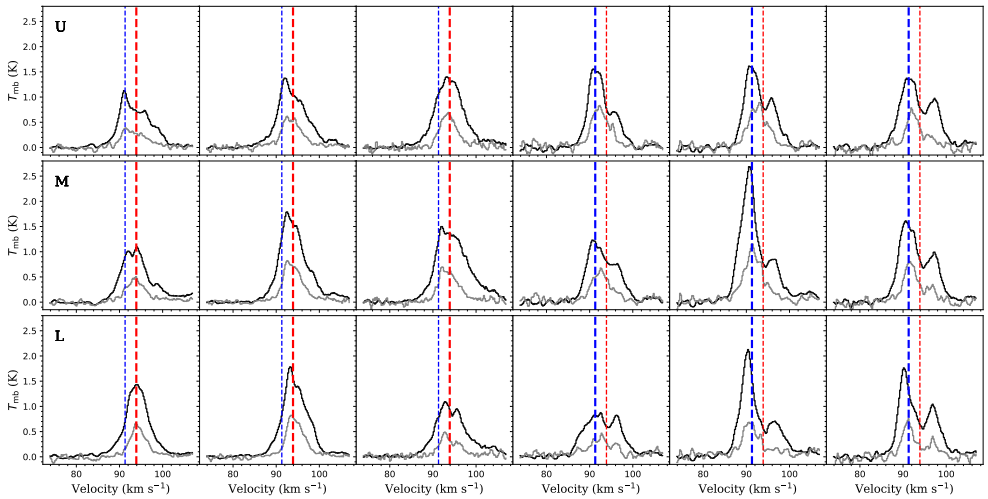

Fig. 13. Average spectrum of the main line of CCH *hfs* component $1_{2,2}$–$0_{1,1}$ (black line) and the satellite line $1_{1,1}$–$0_{1,0}$ (gray line, the intensity is artificially enlarged by three times for comparison) along the three PV cuts U, M, L. From left to right, the spectra are arranged from northeast to southwest along the cuts. The blue and red dashed lines follow that in Fig. 10.

level parental structures. Since the `dendrogram` algorithm works optimally for 2D hierarchical structures, after this initial step, we then generated clusters of the 'leaves' by merging adjacent 'leaves' that have a position distance that is less than the square root of the `min_npix`; specifically, this is done by using the linkage matrix and `fcluster` method in `scipy.cluster` module with a distance threshold. These clusters can then be regarded as representing independent, compact structures from the 3D PPV cube. This method essentially means that we do not distinguish cores by the emission difference in the velocity axis as long as they are located in similar projected positions. The parameters of the extracted compact structures are listed in Tables 6–7. The locations of the extracted structures are marked in Fig. 14. Hereafter, we refer to these compact structures as NH_2D cores.

The average spectra towards all the identified cores are shown in Figs. D.1–D.2. We used one- and two-component *hfs* fits to describe the observed line profiles and the parameter uncertainties are estimated by MCMC method (Appendix D). Considering a gas temperature of 50 K (upper limit seen by extended CH_3CCH emission), the corresponding sound speed is $\sim$0.42 km s^{-1}. Based on the linewidths, these NH_2D cores can be classified into two categories, ones having borad, supersonic linewidth ($\sigma_v \gtrsim 2c_s = 0.85$ km s^{-1}), and the others having narrow, only subsonic to transonic line-width component(s) ($\sigma_v \lesssim 2c_s = 0.85$ km s^{-1}).

Assuming a uniform density profile, the virial mass of NH_2D cores can be estimated by $M_{vir} = \frac{5\sigma_v^2 R}{G}$, with σ_v obtained from the *hfs* fits and R the effective radius defined by the core area from the `dendrogram` source extraction. For NH_2D cores that have two velocity components, we used σ_{narrow} as σ_v, assuming these narrow linewidth structures are stabilised. The derived excitation temperature T_{ex} and the optical depth τ_m of the main line, and the M_{vir} are also listed in Tables 6–7. The virial mass of

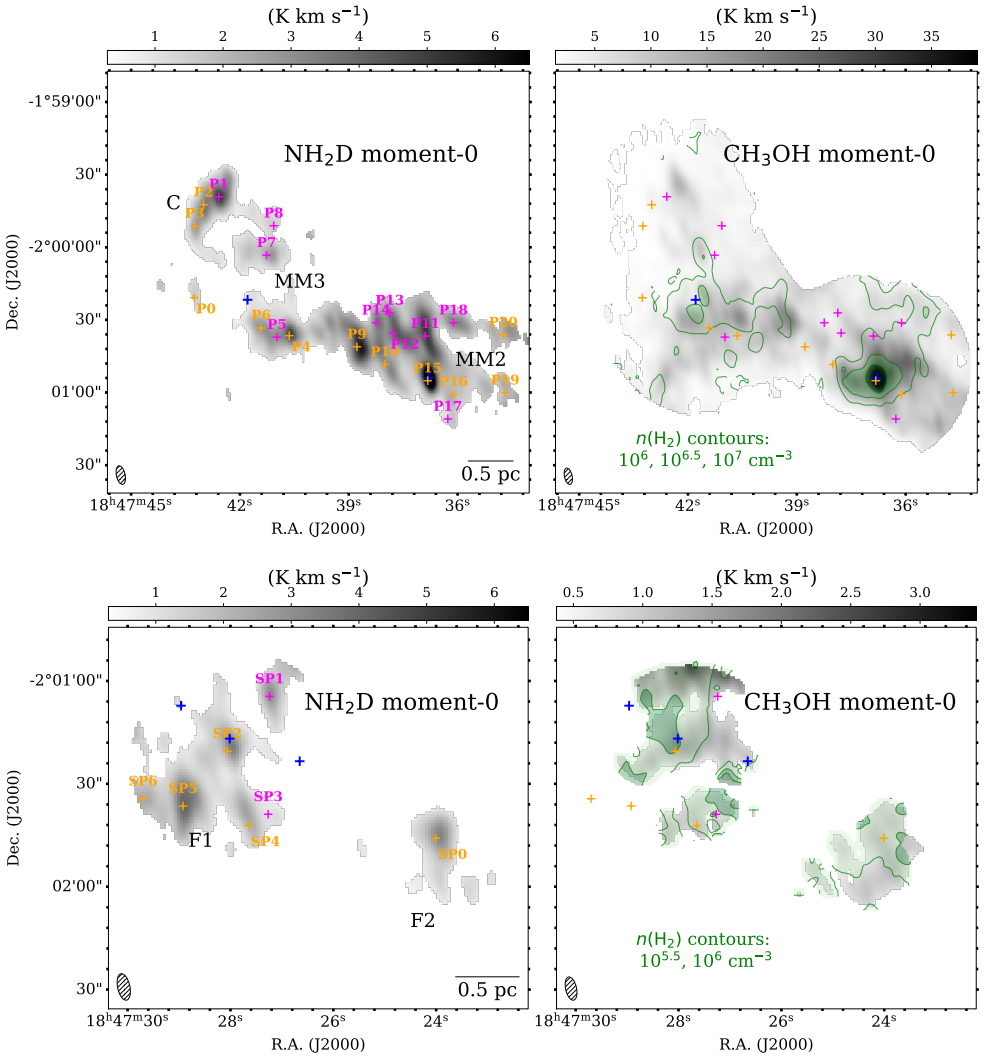

Fig. 14. Integrated intensity map of NH_2D line emission of clumps MM2, MM3, and C (colourscale, of velocity range 80–115 km s^{-1}) are shown in the upper-left panel and marked with locations of NH_2D cores by crosses of different colours. The orange crosses indicate the cores which have a σ_v>0.85 km s^{-1} velocity components and magenta crosses represent cores that only have narrow velocity components, $\sigma_v \lesssim 0.5$ km s^{-1}. Integrated intensity map of CH_3OH 2(0,2)–1(0,1) line (colourscale, of velocity range 85–100 km s^{-1}) overlaid by contours of n(H_2) map (green) shown in the upper-right panel. In both plots, the blue crosses mark the position of the peak intensity of the 3 mm continuum of clumps MM2 and MM3. Lower panels: same as the upper panels, but for the clumps F1 and F2. In both plots, the blue crosses mark the position of the three cores in the 3 mm continuum of clump F1 (as in Fig. 2, right panel).

NH_2D cores range from 11 $M_\odot$ to 300 $M_\odot$. The column densities of NH_2D are derived to be 0.5–5×10^{13} cm^{-2} with a mean value of 2.4×10^{13} cm^{-2}, which are consistent with the column density values of NH_2D observed in massive star-forming regions (e.g. Pillai et al. 2011; Fontani et al. 2015).

5. Discussion

5.1. Gas dynamics dominated by shock activities in massive clumps in W43-main

Previous single-dish observations revealed wide-spread emission of SiO (2–1) throughout the ridges of the 'Z-shaped' structures of W43-main, which is interpreted as arising from low-velocity shocks created by cloud collisions (Nguyen-Luong et al. 2013, see also Louvet et al. 2016 for interferometric observations towards clump MM1). However, there is an ambiguity as to whether the detected low-velocity SiO emission originates from outflows of embedded YSOs (or outflowing gas mixing back to the cloud) or cloud collisions. Jiménez-Serra et al. (2010) found that SiO emission towards an infrared dark cloud composes of an extended low-velocity (line-width~0.8 km s^{-1}) component, which is interpreted as a result of the following scenarios: 1) large-scale shock induced at the formation of the cloud; 2) outflows of a population of low-mass protostars; and 3) recently processed gas by the magnetic precursor of young magneto-hydrodynamic shocks (Jiménez-Serra et al. 2004). In our target clumps, Nony et al. (2023) resolved numerous outflow features from ~0.015 pc resolution observations originating from embedding cores in MM2 and MM3, which may as well be accompanied by SiO emission (Towner et al. 2024). Despite the possible confusion, in Sect. 3.3 we show that the ~0.1 pc scale SiO emission is distributed nearly continuously across the region encompassing the three clumps, hinting at the existence of a global origin from large-scale shocks, together with contribution from multiple outflows of both high-mass and low-mass protostars.

The spatio-kinematic offsets between different tracers have been suggested as indicator of cloud-cloud collision or merging for early-stage clouds (Jiménez-Serra et al. 2010; Henshaw et al. 2013; Bisbas et al. 2018; Priestley & Whitworth 2021). On the PV diagrams, broad bridging features between two velocity components (e.g. Haworth et al. 2015; Priestley & Whitworth 2021), as well as peculiar 'V-shaped' structures (e.g. Takahira et al. 2014; Fukui et al. 2018) also suggest cloud-cloud collisions. In the case of the studied region, the velocity difference between the two clouds in terms of collision is small (V_{LSR} of 91.3 and 93.9 km s^{-1}). The bridging features are therefore not spatially significant in the velocity domain, but they are present in all tracers that have prominent extended emission, for instance, $H^{13}CO^+$, CCH, HC_3N, and SO, as shown in the PV diagrams of Figs. 11–12. In particular, the broader CCH lines

and the additional more red-shifted velocity component around clump MM2 may reflect the less dense outer layer in the cloud merging process.

Pouteau et al. (2023) revealed that the core mass function inside MM2 and MM3 appear top-heavy and there is an evolutionary trend of pre-stellar versus protostellar core mass function possibly resulting from accretion (Nony et al. 2023). The very dense and turbulent gas is common feature of massive clouds ($\sim$100 $M_\odot$) undergoing collision (Inoue & Fukui 2013; Fukui et al. 2016). Indeed, besides the central regions of MM2 and MM3, where the most massive cores reside in, the secondary dense gas enhancements probed by CH_3OH (2–1) lines are also correlated with line wings of SiO emission, as shown in Fig. 9. Although the terminal velocities of the SiO emission are relatively moderate, these excessive velocity wings likely result from the outflow activities from the embedding protostellar cores, especially in clump MM2 and MM3 (Nony et al. 2023). There is also possibility that the much higher velocity SiO wings, which fit better in typical high-velocity jets, still remain undetected with our achieved sensitivity. In any case, this association provides the direct link of supersonic shocks and enhancements of gas density.

The gas kinematics seen from these 0.1–1 pc scale observations is consistent with the larger scale ^{13}CO observations (see also left panel of Fig. 1), which reveal that a 82 km s^{-1} and a 94 km s^{-1} cloud are intersecting at the southern ridge of W43-main (Kohno et al. 2021). Our observations likely represent dense gas tips of the shock-compressed layer close to the red-shifted 94 km s^{-1} cloud.

5.2. Column density of NH_2D and comparison with chemical models

The formation of deuterated ammonia favors cold (<20 K) and dense environments, where the reaction to form H_2D^+ which then transfers to NH_3 to form NH_2D can proceed without the H_2D^+ being destroyed by gas-phase CO (Caselli et al. 2008; Sipilä et al. 2015), as CO depletes by freeze-out onto dust grains (Tafalla et al. 2002; Crapsi et al. 2005). Thus NH_2D emission is expected to preferentially trace the cold and dense gas, for instance, prior to protostellar activity (Pillai et al. 2011) or other heating mechanisms. As can be seen in Fig. 14 (right panel), the NH_2D emission is mostly uncorrelated with CH_3OH emission peak and the localised density enhancements on the $n(H_2)$ map, which are likely induced by intense shocks and subject to heating. Meanwhile, there are widely distributed gas pockets of compact NH_2D emission in MM2, which compose a more extended emission area than that in clump MM3 and C.

We calculated the NH_2D column densities based on the MCMC *hfs* modelling of the two velocity components (Sect. 4), taking into consideration the uncertainties of all the fitted parameters and error propagation. The uncertainty of the column density associated with the broader linewidth component is larger, which is mostly due to the large uncertainty of $\tau_{m\star}$ (as shown in Fig. D.3, which then propagates into uncertainties of $T_{\rm ex}$) as a result of the blending of the satellite components. However, within the uncertainties, we find that the column densities of NH_2D of the broad linewidth component are comparable or even larger than the narrow linewidth counterparts (Fig. 15).

We performed chemical simulations to quantitatively understand the variations of NH_2D abundance in the shock environments typical to W43-main. For this, we used the gas-grain chemical code pyRate, which includes extensive deuterium chemical networks and has been previously used to explain ammonia observations (Sipilä et al. 2013, 2015, 2019a,b). Here, we ran simple zero-dimensional models and adopt three sets of physical conditions characterising pre-shock, shocked, and post-shock gas. Specifically, the gas density, temperature, and extinction level of the gas are listed in Table 5. We assumed the outer envelopes of the three clumps MM2, MM3, and C represent pre-shock gas, having a gas temperature of ~20 K and gas density $10^{4.5}$ cm^{-3}. After the shock processing, the gas density was enhanced, approaching typical densities of $10^{5.5}$ cm^{-3}, as probed by CH_3OH lines (Sect. 3.2.2), together with an elevated while moderate temperature of ~40 K, as seen by H_2CS (Sect. 3.2.1). We also assumed the post-shock gas efficiently cools down to a temperature similar to pre-shock gas while the gas density maintains the high level. The extinction levels are estimated from the $N(H_2)$ map shown in Fig. 1 (middle panel), namely, the environmental extinction of the clumps shielding the external UV radiation.

Table 5. Physical parameters used for three sets of chemical models in this study.

	$n(H_2)$ cm^{-3}	$T_{\rm dust}$ [(a)] K	$A_{\rm v}$ $(1.1\times10^{-21} N_{\rm H_2,env})$
Pre-shock gas	$10^{4.5}$	20	30
Shocked gas	$10^{5.5}$	40	160
Post-shock gas	$10^{5.5}$	20	160

Notes. [(a)] We assume the gas temperature is equal to dust temperature.

We ran two different sets of chemical models. In the first set, the three physical conditions were allowed to develop independently for 0.1 Myr, from the same set of (mostly atomic) initial abundances (Sipilä et al. 2019a). We chose 0.1 Myr for the chemicals evolution epoch as it is a typical timescale of the lifetime of the massive protostellar phase for an object of luminosity 10^4–10^5 $L_\odot$ (e.g. Mottram et al. 2011), which is also consistent with the longest formation timescale we estimate assuming shock-enhanced accretion to form the stablised NH_2D cores (Sect. 5.4). This set of static chemical models allows us to spot the variation of NH_2D abundance that is solely determined by the three distinct physical conditions. The resulting evolution of the NH_2D abundance is shown in Fig. 16, together with that of the main isotopologue NH_3. The lowest NH_2D abundances are seen in the shocked gas and the highest abundances in the post-shock gas: these results are sensible given the favored conditions for deuteration, namely, a high-density and low-temperature environment. The abundance in the shocked gas is smaller but still comparable to that of the pre-shock gas in the first 0.01 Myr of evolution in this set of chemical models.

In the second set of chemical model, we considered the evolution of the three conditions consecutively: the initial stage of pre-shock gas is let evolve for 0.1 Myr, followed by evolution in the shock stage for another 0.1 Myr, which adopts the end result of the first stage as initial abundances for all the species and, finally, another 0.1 Myr with post-shock conditions with initial abundances collected again from the shock stage. Figure 17 shows the results of this simulation: there is drastic decrease of the abundances when the shock conditions kick in and also a steady increment in the beginning of the post-shock stage. In fact, after the first ~0.03 Myr in the post-shock stage, the NH_2D abundance achieves and then maintains the highest level, among all epochs. The observed comparable or even higher NH_2D column densities associated with the broader linewidth component is compatible with the chemical model predictions: we are likely probing the post-shock enhancement of NH_2D with the broad

Table 6. Properties of `dendrogram` extracted NH_2D cores that reside in clumps MM2, MM3, and C.

Core	RA (J2000)	Dec (J2000)	$R_{\rm eff}{}^{(a)}$ (pc)	$\Delta V^{(b)}$ (km s^{-1})	$V_{\rm c}{}^{(b)}$ (km s^{-1})	$\tau_{\rm m}$	$T_{\rm ex}$ (K)	$N_{\rm NH_2D}$ $\times10^{13}$ (cm^{-2})	$M_{\rm vir}{}^{(c)}$ ($M_\odot$)
P0	$18^h47^m43\overset{s}{.}20$	$-02°00'20\overset{''}{.}0$	0.10	1.5(0.1)	96.0(0.1)	0.9(0.0)	3.0(0.0)	11.2(2.3)	48.5
P1	$18^h47^m42\overset{s}{.}52$	$-01°59'38\overset{''}{.}3$	0.13	1.6(0.5),1.0(0.1)	91.1(0.4),90.2(0.0)	0.4(0.2),0.6(0.1)	3.5(0.5),4.7(0.4)	2.4(2.3),2.2(0.8)	26.5
P2	$18^h47^m42\overset{s}{.}94$	$-01°59'41\overset{''}{.}6$	0.10	2.1(0.5),1.2(0.3)	90.9(0.2),90.9(0.1)	0.3(0.2),0.4(0.2)	3.8(0.9),4.5(1.0)	2.8(3.2),1.3(1.4)	28.7
P3	$18^h47^m43\overset{s}{.}18$	$-01°59'50\overset{''}{.}3$	0.16	1.8(0.2),1.1(0.5)	90.7(0.1),95.7(2.5)	0.4(0.2),0.4(0.3)	4.2(0.9),3.1(0.4)	2.4(2.8),2.2(1.8)	41.8
P4	$18^h47^m40\overset{s}{.}58$	$-02°00'35\overset{''}{.}7$	0.08	3.5(0.9),0.8(0.1)	93.2(0.3),96.8(0.0)	0.5(0.2),0.8(0.1)	3.4(0.4),3.7(0.1)	7.6(6.7),4.7(1.7)	11.1
P5	$18^h47^m40\overset{s}{.}92$	$-02°00'36\overset{''}{.}3$	0.12	1.5(0.8),0.8(0.1)	93.2(0.2),96.8(0.0)	0.7(0.2),0.7(0.2)	3.4(0.2),3.7(0.3)	5.8(4.7),3.2(2.2)	16.4
P6	$18^h47^m41\overset{s}{.}35$	$-02°00'32\overset{''}{.}4$	0.12	3.7(0.8),0.9(0.1)	94.2(0.4),96.4(0.0)	0.4(0.2),0.4(0.2)	3.2(0.3),4.3(0.8)	6.6(5.0),1.1(1.2)	20.1
P7	$18^h47^m41\overset{s}{.}21$	$-02°00'02\overset{''}{.}4$	0.11	0.9(0.0)	95.5(0.0)	0.8(0.0)	3.5(0.0)	6.1(0.8)	19.9
P8	$18^h47^m41\overset{s}{.}01$	$-01°59'50\overset{''}{.}2$	0.07	1.0(0.0)	95.2(0.0)	0.5(0.1)	3.8(0.3)	2.1(1.1)	14.7
P9	$18^h47^m38\overset{s}{.}72$	$-02°00'40\overset{''}{.}2$	0.10	3.7(1.0),0.8(0.1)	93.6(0.6),92.1(0.0)	0.4(0.2),0.8(0.1)	3.3(0.4),4.4(0.2)	7.0(6.0),3.3(1.1)	11.8
P10	$18^h47^m37\overset{s}{.}95$	$-02°00'47\overset{''}{.}5$	0.11	2.6(1.3),0.8(0.1)	94.0(1.0),94.0(0.0)	0.5(0.3),0.5(0.2)	3.1(0.2),4.7(0.9)	5.4(4.6),1.2(1.2)	17.3
P11	$18^h47^m36\overset{s}{.}83$	$-02°00'35\overset{''}{.}8$	0.15	3.8(1.2),0.8(0.1)	91.3(0.7),92.6(0.0)	0.5(0.3),0.6(0.1)	3.1(0.2),5.0(0.5)	8.2(6.1),1.7(0.9)	22.9
P12	$18^h47^m37\overset{s}{.}72$	$-02°00'34\overset{''}{.}6$	0.09	1.1(0.0)	92.2(0.0)	0.7(0.0)	4.5(0.1)	3.5(0.5)	23.2
P13	$18^h47^m37\overset{s}{.}81$	$-02°00'26\overset{''}{.}2$	0.13	1.5(0.1)	92.2(0.0)	0.6(0.1)	3.9(0.2)	4.1(1.3)	58.0
P14	$18^h47^m38\overset{s}{.}19$	$-02°00'30\overset{''}{.}3$	0.09	1.6(0.1)	91.9(0.0)	0.7(0.1)	3.8(0.1)	6.2(1.4)	48.0
P15	$18^h47^m36\overset{s}{.}77$	$-02°00'54\overset{''}{.}2$	0.08	5.6(0.9),1.2(0.2)	89.8(0.2),88.0(0.1)	0.5(0.2),0.8(0.2)	4.0(0.5),3.2(0.1)	12.5(11.3),7.7(4.5)	24.6
P16	$18^h47^m36\overset{s}{.}05$	$-02°00'59\overset{''}{.}9$	0.12	1.8(0.9),1.4(0.4)	91.0(0.5),92.3(0.2)	0.5(0.3),0.3(0.2)	3.2(0.3),4.0(0.8)	3.7(3.5),1.4(1.6)	51.4
P17	$18^h47^m36\overset{s}{.}21$	$-02°01'10\overset{''}{.}0$	0.12	1.7(0.7),1.2(0.3)	91.9(0.4),90.5(0.1)	0.3(0.2),0.4(0.2)	3.5(0.5),3.7(0.5)	2.5(2.6),2.2(2.2)	36.9
P18	$18^h47^m36\overset{s}{.}06$	$-02°00'30\overset{''}{.}3$	0.11	1.9(0.8),0.8(0.1)	92.8(0.5),92.0(0.1)	0.5(0.3),0.6(0.2)	3.2(0.3),3.9(0.4)	4.7(4.0),2.4(2.0)	15.7
P19	$18^h47^m34\overset{s}{.}63$	$-02°00'59\overset{''}{.}2$	0.10	3.7(0.7)	91.8(0.2)	0.1(0.6)	5.2(13.2)	0.8(8.1)	296.4
P20	$18^h47^m34\overset{s}{.}68$	$-02°00'35\overset{''}{.}3$	0.07	1.4(0.1)	92.9(0.1)	0.8(0.1)	3.3(0.1)	8.5(3.4)	31.1

Notes. $^{(a)}R_{\rm eff}$ is the effective radius of the core area, i.e. $\pi\ R_{\rm eff}{}^2$ = Area; $^{(b)}\Delta V$ and $V_{\rm c}$ are the FWHM linewidth and centroid velocity from Gaussian line profile, listed for two-component fits and one-component fit accordingly; $^{(c)}$For the two-component fits, $M_{\rm vir}$ is calculated using the narrower linewidth.

Table 7. Properties of `dendrogram` extracted NH_2D cores that reside in clump F1 and F2.

Core	RA (J2000)	Dec (J2000)	$R_{\rm eff}{}^{(a)}$ (pc)	$\Delta V^{(b)}$ (km s^{-1})	$V_{\rm c}{}^{(b)}$ (km s^{-1})	$\tau_{\rm m}$	$T_{\rm ex}$ (K)	$N_{\rm NH_2D}$ $\times10^{13}$ (cm^{-2})	$M_{\rm vir}{}^{(c)}$ ($M_\odot$)
SP0	$18^h47^m23\overset{s}{.}95$	$-02°01'45\overset{''}{.}0$	0.21	2.4(0.2)	189.3(0.1)	0.5(0.1)	3.3(0.1)	5.7(2.2)	244.8
SP1	$18^h47^m27\overset{s}{.}18$	$-02°01'03\overset{''}{.}6$	0.12	2.1(1.5),1.4(0.2)	192.3(1.2),195.7(0.1)	0.5(0.3),0.5(0.2)	3.0(0.2),3.8(0.6)	4.8(4.5),2.8(2.8)	48.3
SP2	$18^h47^m28\overset{s}{.}00$	$-02°01'19\overset{''}{.}6$	0.10	3.0(0.8),1.1(0.1)	197.1(0.6),198.1(0.0)	0.4(0.2),0.5(0.2)	3.2(0.3),4.1(0.6)	5.2(3.7),1.8(1.5)	24.0
SP3	$18^h47^m27\overset{s}{.}21$	$-02°01'38\overset{''}{.}0$	0.12	1.1(0.1)	197.7(0.0)	0.6(0.1)	3.3(0.1)	3.7(1.1)	29.0
SP4	$18^h47^m27\overset{s}{.}59$	$-02°01'41\overset{''}{.}3$	0.18	5.5(1.7)	194.9(0.1)	0.1(0.7)	4.2(10.2)	1.6(20.2)	1156.2
SP5	$18^h47^m28\overset{s}{.}86$	$-02°01'35\overset{''}{.}6$	0.14	1.1(2.6),0.8(0.1)	194.8(1.0),198.2(0.0)	0.6(0.3),0.7(0.1)	3.2(0.3),4.0(0.2)	3.0(7.6),2.7(1.1)	19.8
SP6	$18^h47^m29\overset{s}{.}64$	$-02°01'33\overset{''}{.}5$	0.10	2.8(1.6),1.0(0.2)	195.9(1.0),199.2(0.1)	0.5(0.3),0.5(0.3)	3.0(0.2),3.4(0.4)	6.1(4.8),2.1(2.0)	21.2

Notes. $^{(a,b,c)}$Same as Table 6.

linewidth velocity component. We acknowledge that our current investigation solely allows us to examine NH_2D column densities. However, it is important to highlight that the chemical models provide predictions for NH_2D abundance, introducing a non-direct one-to-one comparison between the observed data and model predictions. On the other hand, the narrow linewidth velocity components observed may predominantly signify pre-shock gas or potentially post-shock gas from the preceding shock event (formed in the previous, lower density-enhanced environment), which have undergone decay through turbulence dissipation. In the context of core formation within shock conditions, uncertainty arises regarding whether these cores serve as remnants from the shock waves preceding the current one or represent the concluding outcomes of the second-to-last shock wave. The centroid velocities of the narrow linewidth components are more widely distributed and appear oscillatory (see more in Sect. 5.3) compared to that of the SiO, indicating that their location in spatial and velocity domain is further away from the current shock front.

Similar results of the enhancement of N_2H^+ deuterium fractionation in post-shock region is suggested in Cosentino et al. (2023) towards an infrared-dark cloud adjacent to a supernovae remnant, as an outcome of the fast chemistry in density-enhanced gas. In addition, thermal heating and/or shock sputtering that cause desorption of the grain-surface NH_2D may also contribute to the observed enhancement. We also note that in our present simulations, which do not take into account the actual shock events, the temperature is never high enough for efficient thermal NH_3 or NH_2D desorption.

5.3. Kinematics of NH_2D cores

To understand the origin of the NH_2D cores from a kinematic perspective, we compare the position-velocity distribution of the

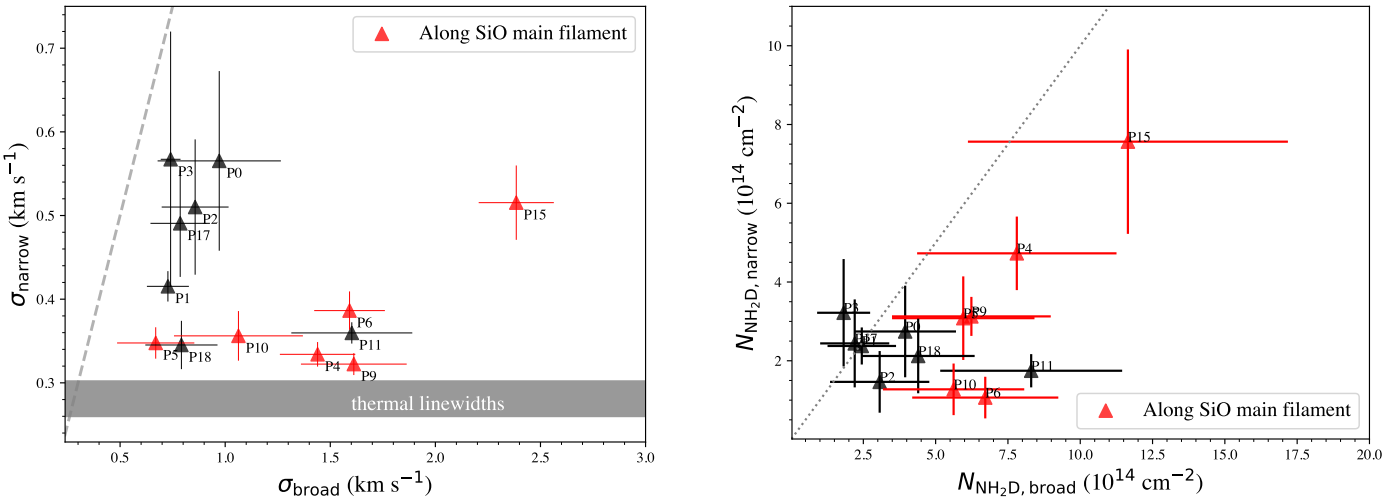

Fig. 15. Relation between the narrow linewidths and broad linewidths of spectra of NH_2D cores residing in clumps MM2, MM3, and C (left). The gray dashed line indicates equal linewidths. NH_2D cores that reside along the main filament of SiO emission are marked in red, and others in black. The shaded region indicates the thermal linewidths based on $T_{\rm rot}$ map derived by CH_3CCH lines (Sect. 3.2). Comparison between column density of NH_2D of the narrow linewidth and broad linewidth components (right). The gray dashed line indicates equal column density.

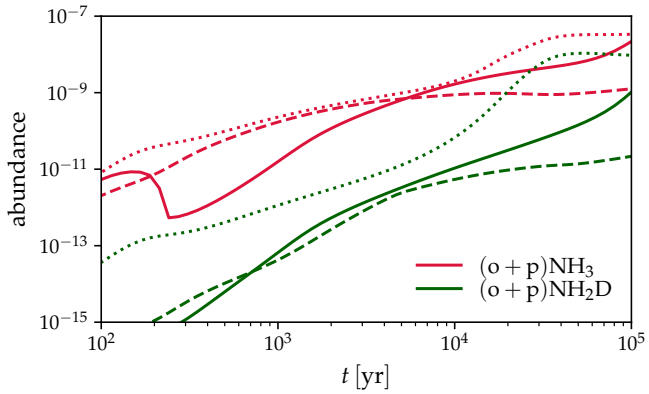

Fig. 16. Abundance of (ortho + para) NH_3 and NH_2D in shock environment, predicted by chemical models. Static physical conditions of pre-shock (solid line), shocked (dashed line), and post-shock gas (dotted line), characterised the by gas density and temperature, and extinction levels listed in Table 5.

NH_2D cores with respect to emission of SiO (2–1), $H^{13}CO^+$ (1–0), and CCH $1_{2,2}$–$0_{1,1}$ lines. Following three positional cuts that are illustrated in Fig. 18, we show the PV diagrams of CCH and SiO lines in the right panel (in colourscale), in which the peak velocities of $H^{13}CO^+$, SiO, and CCH are shown as reference lines. The centroid velocities marking the position of NH_2D cores on the velocity axis are derived from the one-component or two-component *hfs* fits, shown as red and green markers, respectively. In the PV diagrams, the zero offsets correspond to the northernmost position of the three cuts. The centroid velocities of the broader velocity component (darker green markers) of NH_2D cores mostly coincide with the peak velocities of SiO, whereas centroid velocities of the narrow velocity components or of the one-component fit can either be blue- or red-shifted with respect to that of SiO. This indicates that the broader line-widths of NH_2D are more closely connected to the shock activities. Although associated with large uncertainties, the column density of the broader linewidth components also appear to be larger than their narrow linewidth counterparts, as shown in Fig. 15 (right panel). These gas components are dominated by cloud collisions, whose turbulent energy has not been dissipated, despite their spatial closeness (along the line of sight) with the dense gas ridge (main filament of SiO) linking MM2 and MM3.

To further illustrate the relation of the NH_2D cores and the bulk gas structures in these massive clumps, we show in Fig. 19 the distribution of velocity offsets between the centroid velocities of NH_2D lines and the peak velocity of other molecular lines (SiO, CCH, CH_3OH, $HC^{15}N$, HC_3N, and $H^{13}CO^+$). All the lines are extracted and averaged from the position of the NH_2D cores. It can be seen that the centroid velocities of the broad-linewidth velocity components of NH_2D cores are more consistent with the peak velocities of SiO, CCH and CH_3OH, with velocity offsets centralised around zero. Interestingly, most of the centroid velocities of the narrow-line-width components are red-shifted or blue-shifted compared to peak velocities of $H^{13}CO+$, HC_3N, or $HC^{15}N$. From the PV diagrams in Fig. 18, this behaviour can also be seen clearly, and the distribution of the centroid velocity of the narrow-line-width components along the cuts appear oscillatory with respect to the peak velocities of $H^{13}CO+$: they alternate from being blue-shifted to to red-shifted and blue-shifted again, from north to south. The oscillatory distribution in intensity space is resolved in simulations of cloud-cloud collisions in Takahira et al. (2014, 2018), which appear orthogonal to the collision axis and may represent outer gas layers perturbed by the shock activities.

We make a comparison of the line-widths of the two velocity components of the NH_2D cores identified in clumps MM2, MM3, and C, as shown in the left panel of Fig. 15. We classify the NH_2D cores into two categories: those that are located close ($\lesssim$0.2 pc) to the main filament of SiO (in-between the thick red and blue lines in the upper panel of Fig. 9, mainly the dense gas ridge of MM2 and MM3) and those that are further away. Apparently the difference between the broad and narrow linewidth in the second class is smaller, while the cores along the SiO main filament have narrow line-width comparable to the sonic value. There is a large difference between the broad and narrow linewidth of the two velocity components.

The broad linewidths NH_2D emission in high mass star-forming regions have been observed with single-dish observations (e.g. Fontani et al. 2015; Li et al. 2023). However,

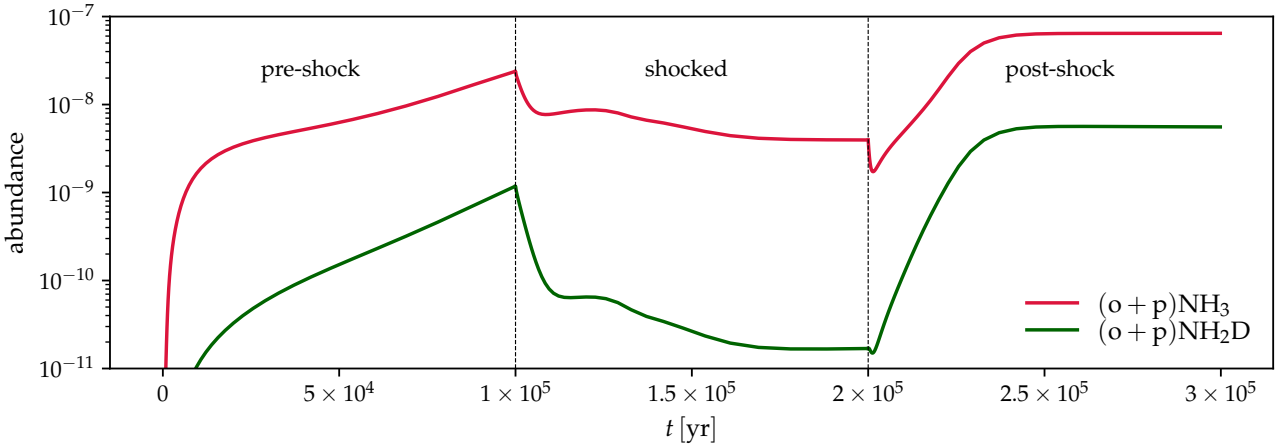

Fig. 17. Evolution of the abundance of (ortho + para) NH_3 and NH_2D in shock environment, predicted by chemical models. Similar to Fig. 16, three conditions of pre-shock, shocked and post-shock gas are characterised by gas density and temperature, and extinction levels listed in Table 5. Contrary to the models shown in Fig. 16, each physical state is evolved for 0.1 Myr, with the latter two states having abundance levels initialised by the end values of the prior state.

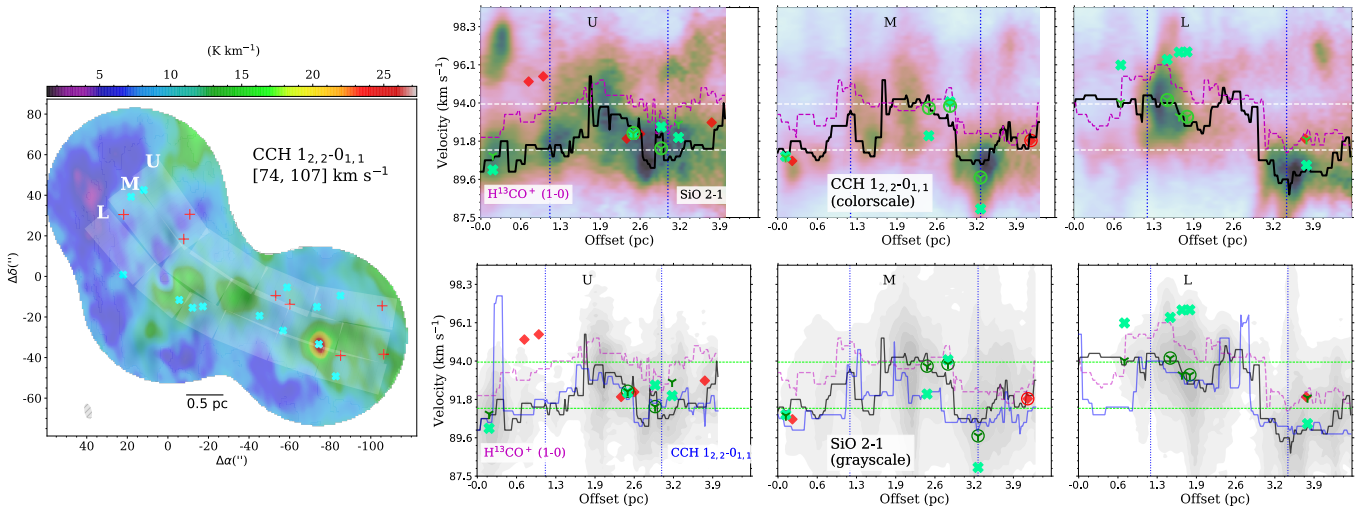

Fig. 18. Position of NH_2D cores on CCH integrated intensity map (left). Red crosses mark the NH_2D cores that have two velocity components, and cyan crosses mark those of one velocity component. Relation of NH_2D cores with CCH and $H^{13}CO^+$ emission (right), shown as position-velocity diagram. The three panels are position-velocity cuts along the shaded bands U, M, and L in left figure. Peak velocities along the spatial offset for different lines are shown as dashed or solid lines with respective colours ($H^{13}CO^+$: magenta, SiO: black, CCH: blue). Background colour scale shows the PV diagram of CCH (in upper panel) and SiO (in lower panel). NH_2D cores with two velocity components are marked as green X and three-branched triangles, and those with only one velocity component are shown as red diamonds. NH_2D cores that have σ_v>0.85 km s^{-1} are marked with an additional hollow circle around the aforementioned markers.

compared to other NH_2D cores identified by interferometric observations in high-mass star forming regions which mostly show narrow linewidths ($\sigma_v \lesssim 0.5$ km s^{-1}, Pillai et al. 2011; Zhang et al. 2020; Li et al. 2021) and also H_2D^+ cores (Redaelli et al. 2021), our discovery of supersonic linewidth NH_2D gas components appear peculiar and may reflect a recent shock processing of their embedded massive clumps.

5.4. Fragmentation of the NH_2D cores

As an assessment of the possible fragmentation process leading to the formation of the NH_2D cores, we made comparisons between the observed core separation, namely, the distance to each core's nearest neighbour, core virial mass, and the critical length and mass scales based on Jeans fragmentation predictions. Towards the region of clumps MM2, MM3, and C, we adopted the clump envelope gas density and the turbulent line-width (the broader velocity component) as one set of parameters, while the core gas density and thermal line-widths were taken as the other for the Jeans fragmentation assessment. We regard these two parameter sets as representing roughly the properties of large-scale clump bulk gas, and localised dense gas. The core densities are yielded from the CH_3OH derived n(H_2) maps, and the envelope density is adopted as a characteristic bulk gas density of 10^5 cm^{-3} for these clumps (Lin et al. 2016). Takahira et al. (2018) found that the core formation from cloud-cloud collisions is dominated by accretion of shocked gas. We regarded the core virial masses based on estimate from the narrow linewidth components represent typical core mass formed in this shock environments (although we note in Sect. 5.2 that these narrow linewidth objects may represent cores formed in last shock activities) and following the formulations in Takahira et al. (2018), we can then calculate core the formation timescale by assuming a characteristic accretion

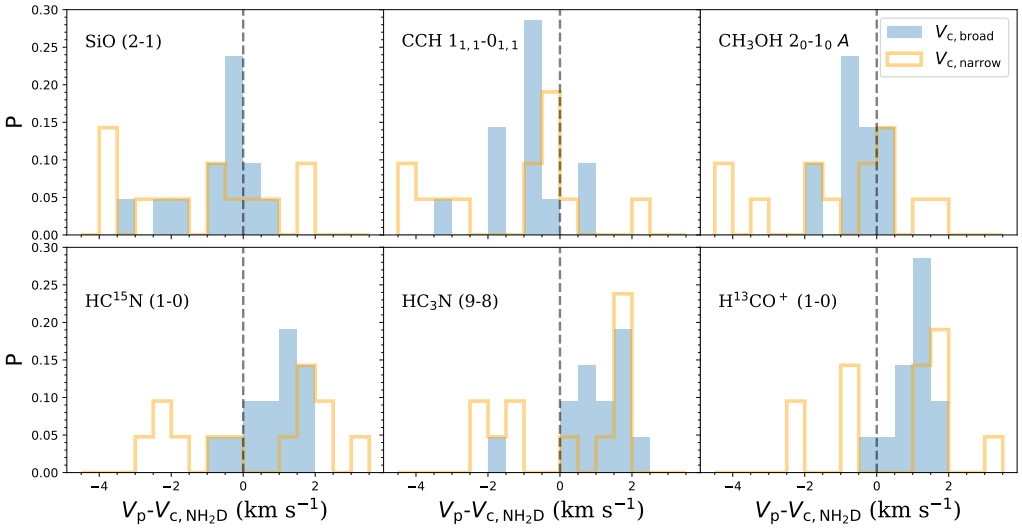

Fig. 19. Probability distribution of velocity offset between peak velocities of multiple lines with respect to the centroid velocity of NH_2D lines of NH_2D cores. The peak velocity, V_p, is given by the corresponding molecular line noted in upper left corner of each subplot; V_{c,NH_2D} indicate the centroid velocity of the broad-linewidth component or the narrow-linewidth component of the two-component fits to NH_2D lines (Fig. D.1).

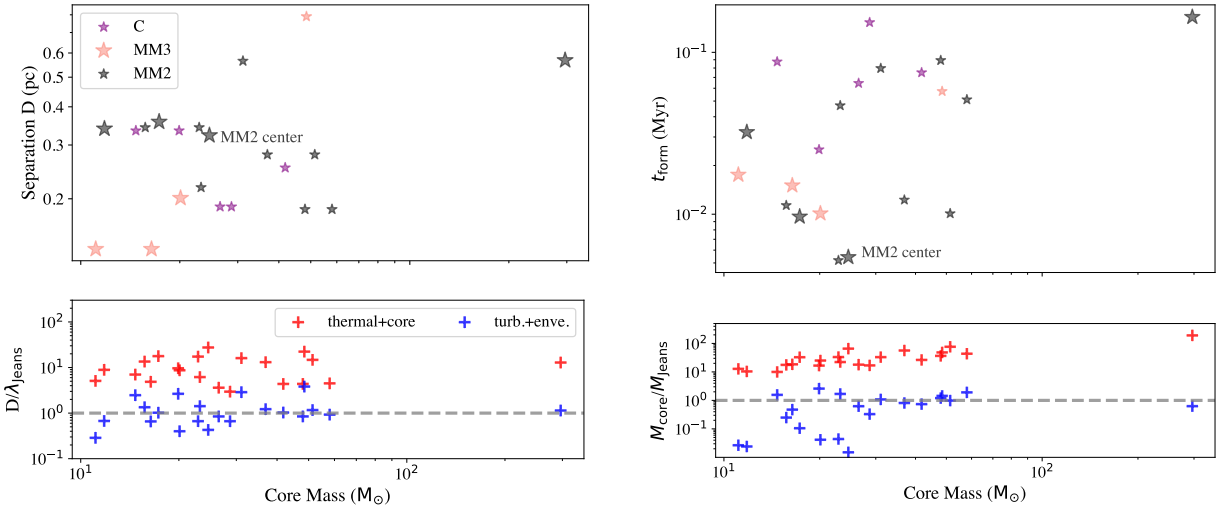

Fig. 20. Properties of NH_2D cores. Left panel: relation of mass of NH_2D cores (virial mass) in G30.7 and their separation (to the nearest neighbor) (upper panel); the ratio between the separation and the critical length scale estimated from Jeans fragmentation (lower panel). Right panel: relation of mass of NH_2D core (virial mass) and formation timescale (upper panel). The ratio between the separation and the critical mass scale estimated from Jeans fragmentation (lower panel). The plots in the right panel share the same labels as in the legend of the left panel. In both upper plots, the cores that have $\sigma_v > 0.85$ km s^{-1} in at least one velocity component is shown as enlarged markers.

rate and isotropic infall. The accretion rate is estimated by $\dot{M} = \pi r_{acc}^2 \sigma_{eff} \rho_{acc}$, where $r_{acc} = \frac{2GM_{core}}{\sigma_{eff}^2} + r_{core}$, and ρ_{acc} is the average ambient gas density (within r_{acc}. excluding the core). Taking ρ_{acc} from the $n(H_2)$ map and M_{core} as M_{vir}, σ_{eff} as the σ_v as that of the broad velocity component, we calculate a core formation timescale as $t_{form} = \frac{M_{vir}}{\dot{M}}$. In the left panel of Fig. 20, we show the relation between the core virial mass and separation and the ratio of the separations to the estimated critical Jeans lengths. In the right panel of Fig. 20, the comparisons between core virial mass and core formation timescale and the ratio of virial masses and critical Jeans masses are shown.

The observed separation between cores and the core virial mass does not particularly favour predictions of either turbulent fragmentation of the envelope or thermal fragmentation of the in-situ dense gas. In general, the separations seem to be closer to current predictions for turbulent fragmentation of the envelope, but the mass scales lie in-between the two scenarios. We note again that the virial mass estimated from the narrow linewidth NH_2D line is used as a proxy for core mass, which may be several times underestimated (Pillai et al. 2011; Zhang et al. 2020), compared to the dust mass. This will make the difference between the core mass and that of the turbulent fragmentation smaller, but still cannot single out this scenario. The formation timescale, t_{form}, of these NH_2D cores is weakly correlated with core mass, with a Spearman correlation coefficient of 0.37 (p-value ~0.1), ranging between 1×10^3–10^5 yr.

6. Conclusion

We conducted 3 mm NOEMA and IRAM 30m observations towards massive clumps in W43-main molecular complex, with the primary goal of constraining the physical structures. The clumps are residing in a highly turbulent environment and may be formed coevally as indicated by their similar luminosity to mass ratios. Our results are summarised as follows:

– We derived the rotational temperature maps using H_2CS (3–2), CH_3CCH (6–5), (5–4), and C_2H_3CN (9–8) lines as thermometers, and the hydrogen volume density maps from the CH_3OH (2–1) lines. The gas temperatures of clump

MM3 show the most centrally peaked profile, reaching 130 K in the center and levelling to 30 K at a radius of 0.3 pc. Clump MM3 has temperatures of ~40–50 K at the peak of the line emission, which is offset from the peak of the 3 mm continuum emission. There are two distinct velocity components towards clump C, one with bulk temperature 25–35 K and one with $\lesssim$20 K, as traced by CH_3CCH. The two rotational temperatures derived by H_2CS show less contrast, which may indicate that H_2CS is mostly tracing the lower density, shocked envelope gas surrounding the CH_3CCH emission.

- The position-velocity maps of SiO (2–1) and CH_3OH $5_{1,5}$–$4_{0,4}$ along the main filament linking MM2 and MM3 show multiple double-wing velocity profiles, with linewidths $\lesssim$8 km s^{-1}. The line wings in CH_3OH $5_{1,5}$–$4_{0,4}$ all have counterparts in SiO (2–1) profiles, while SiO (2–1) exhibits additionally single blue-shifted line wings, reaching terminal velocities of $\gtrsim$10 km s^{-1} around the V_{LSR}. With possible confusion from outflows driven by embedded clusters in the formation, the relatively narrow-wing, spatially extended and highly asymmetric SiO line emission likely arises from cloud collisions. Double-peaked CCH (1–0) emission likely traces the larger scale merging clouds of less dense gas.
- The gas density enhancements ($\gtrsim 10^6$ cm^{-3}) seen by CH_3OH across clumps MM2, MM3 and C are strongly correlated with SiO line wings. The most significant density enhancements (~10^7 cm^{-3}) likely represent strongly self-gravitating regions that are actively forming stars. The secondary density enhancements are more extended and widely distributed, showing the direct link between dense gas concentration and the impact of supersonic turbulence.
- Systematic velocity shifts are observed among HC_3N, $H^{13}CO^+$, SO, H_2CS, and SiO, CH_3OH, CCH, CH_3CCH along the main filament. SiO peak velocities align well with CH_3OH, CCH, and CH_3CCH, while SO and H_2CS consistently exhibit a red-shift of 1 km s^{-1} compared to SiO. HC_3N, $H^{13}CO^+$, and HCN show a further red-shift with a ~2 km s^{-1} difference. The distinct and systematic layering observed among these tracers provides an important evidence of cloud collisions and merging.
- We discover a population of NH_2D cores which can be categorised into two classes: those that lie close to the main SiO filament, having broad, supersonic velocity components of $\sigma_v > 2c_s = 0.85$ km s^{-1}, and the others that are located further away from the main filament, only having narrow velocity component of σ_v~0.5 km s^{-1}, in the range of transonic (~$2c_s$) to subsonic ($\lesssim c_s$) regimes. The enhancement of NH_2D abundance in a shock environment, which peaks in the post-shock gas, is predicted by our chemical models. The NH_2D cores located close to the main filament may represent evolutionary stages still prior or in the stage of turbulence dissipation.
- The virial masses of these NH_2D cores range from 3 to 100 $M_\odot$, estimated by the narrow linewidth component. The existence of these cores may hint at a new generation of stars being formed in the post-shock gas compressed by cloud collisions. The formation timescales of these cores roughly scale with their masses and the fragmentation properties are closer to the turbulent fragmentation of the envelope gas than to the in situ fragmentation of dense gas.

Our results reveal the direct link between shock activities and enhanced gas densities inside these massive star-forming clumps. The broad linewidth 'cold' and high-density gas tracers, such as NH_2D, may possess important information to pin down the relation of new-generation core formation, and timescales of shock activities. Core formation under the shock environment can be quick and chaotic, facilitated by the enhanced accretion of gas channelling and/or local density-driven infall. The prevalence of such systems in favor of massive cluster formation may be revealed by future observations towards a statistically significant sample of massive star-forming clouds.

Acknowledgements. We appreciate the insightful feedback and suggestions from the referee which contributed to refining the manuscript. This work was partly funded by the Deutsche Forschungsgemeinschaft (DFG, German Research Foundation) under SFB 956. H.B.L. is supported by the National Science and Technology Council (NSTC) of Taiwan (Grant Nos. 111-2112-M-110-022-MY3). Y.L. wishes to thank Orsolya Feher and Jérôme Pety for their kind help in the NOEMA data reduction.

References

Anathpindika, S. V. 2010, MNRAS, 405, 1431
Balança, C., Dayou, F., Faure, A., Wiesenfeld, L., & Feautrier, N. 2018, MNRAS, 479, 2692
Balfour, S. K., Whitworth, A. P., Hubber, D. A., & Jaffa, S. E. 2015, MNRAS, 453, 2471
Balfour, S. K., Whitworth, A. P., & Hubber, D. A. 2017, MNRAS, 465, 3483
Bally, J., Anderson, L. D., Battersby, C., et al. 2010, A&A, 518, A90
Bertoldi, F. 1989, ApJ, 346, 735
Beuther, H., Semenov, D., Henning, T., & Linz, H. 2008, ApJ, 675, L33
Bisbas, T. G., Wünsch, R., Whitworth, A. P., & Hubber, D. A. 2009, A&A, 497, 649
Bisbas, T. G., Wünsch, R., Whitworth, A. P., Hubber, D. A., & Walch, S. 2011, ApJ, 736, 142
Bisbas, T. G., Tan, J. C., Csengeri, T., et al. 2018, MNRAS, 478, L54
Blum, R. D., Damineli, A., & Conti, P. S. 1999, AJ, 117, 1392
Brunthaler, A., Menten, K. M., Dzib, S. A., et al. 2021, A&A, 651, A85
Carey, S. J., Noriega-Crespo, A., Mizuno, D. R., et al. 2009, PASP, 121, 76
Carlhoff, P., Nguyen Luong, Q., Schilke, P., et al. 2013, A&A, 560, A24
Caselli, P., Hartquist, T. W., & Havnes, O. 1997, A&A, 322, 296
Caselli, P., Vastel, C., Ceccarelli, C., et al. 2008, A&A, 492, 703
Churchwell, E. 2002, ARA&A, 40, 27
Cortes, P. C., Hull, C. L. H., Girart, J. M., et al. 2019, ApJ, 884, 48
Cosentino, G., Jiménez-Serra, I., Tan, J. C., et al. 2022, MNRAS, 511, 953
Cosentino, G., Tan, J. C., Jiménez-Serra, I., et al. 2023, A&A, 675, A190
Crapsi, A., Caselli, P., Walmsley, C. M., et al. 2005, ApJ, 619, 379
Daniel, F., Faure, A., Wiesenfeld, L., et al. 2014, MNRAS, 444, 2544
Dyson, J. E., & Williams, D. A. 1997, The Physics of the Interstellar Medium (Bristol: Institute of Physics Publishing)
Endres, C. P., Schlemmer, S., Schilke, P., Stutzki, J., & Müller, H. S. 2016, J. Mol. Spectrosc., 327, 95
Faure, A., Lique, F., & Wiesenfeld, L. 2016, MNRAS, 460, 2103
Fontani, F., Busquet, G., Palau, A., et al. 2015, A&A, 575, A87
Fukui, Y., Torii, K., Ohama, A., et al. 2016, ApJ, 820, 26
Fukui, Y., Kohno, M., Yokoyama, K., et al. 2018, PASJ, 70, S44
Fukui, Y., Habe, A., Inoue, T., Enokiya, R., & Tachihara, K. 2021, PASJ, 73, S1
Giannetti, A., Leurini, S., Wyrowski, F., et al. 2017, A&A, 603, A33
Habe, A., & Ohta, K. 1992, PASJ, 44, 203
Haworth, T. J., Shima, K., Tasker, E. J., et al. 2015, MNRAS, 454, 1634
Hennebelle, P., & André, P. 2013, A&A, 560, A68
Henshaw, J. D., Caselli, P., Fontani, F., et al. 2013, MNRAS, 428, 3425
Hill, J. K., & Hollenbach, D. J. 1978, ApJ, 225, 390
Högbom, J. A. 1974, A&AS, 15, 417
Inoue, T., & Fukui, Y. 2013, ApJ, 774, L31
Inoue, T., Hennebelle, P., Fukui, Y., et al. 2018, PASJ, 70, S53
Jiang, X.-J., Liu, H. B., Zhang, Q., et al. 2015, ApJ, 808, 114
Jiménez-Serra, I., Martín-Pintado, J., Rodríguez-Franco, A., & Marcelino, N. 2004, ApJ, 603, L49
Jiménez-Serra, I., Caselli, P., Martín-Pintado, J., & Hartquist, T. W. 2008, A&A, 482, 549
Jiménez-Serra, I., Caselli, P., Tan, J. C., et al. 2010, MNRAS, 406, 187
Kohno, M., Tachihara, K., Torii, K., et al. 2021, PASJ, 73, S129
Kumar, M. S. N., Palmeirim, P., Arzoumanian, D., & Inutsuka, S. I. 2020, A&A, 642, A87
Leurini, S., Schilke, P., Menten, K. M., et al. 2004, A&A, 422, 573
Leurini, S., Schilke, P., Wyrowski, F., & Menten, K. M. 2007, A&A, 466, 215
Li, S., Lu, X., Zhang, Q., et al. 2021, ApJ, 912, L7
Li, Y., Wang, J., Li, J., et al. 2023, MNRAS
Lin, Y., Liu, H. B., Li, D., et al. 2016, ApJ, 828, 32

Lin, Y., Wyrowski, F., Liu, H. B., et al. 2022, A&A, 658, A128
Liow, K. Y., & Dobbs, C. L. 2020, MNRAS, 499, 1099
Louvet, F., Motte, F., Gusdorf, A., et al. 2016, A&A, 595, A122
Mac Low, M.-M., Toraskar, J., Oishi, J. S., & Abel, T. 2007, ApJ, 668, 980
Mezger, P. G., & Henderson, A. P. 1967, ApJ, 147, 471
Mocz, P., & Burkhart, B. 2018, MNRAS, 480, 3916
Molinari, S., Swinyard, B., Bally, J., et al. 2010, A&A, 518, L100
Molinari, S., Merello, M., Elia, D., et al. 2016a, ApJ, 826, L8
Molinari, S., Schisano, E., Elia, D., et al. 2016b, A&A, 591, A149
Möller, T., Endres, C., & Schilke, P. 2017, A&A, 598, A7
Motte, F., Schilke, P., & Lis, D. C. 2003, ApJ, 582, 277
Motte, F., Nguyên Luong, Q., Schneider, N., et al. 2014, A&A, 571, A32
Motte, F., Bontemps, S., & Louvet, F. 2018, ARA&A, 56, 41
Motte, F., Bontemps, S., Csengeri, T., et al. 2022, A&A, 662, A8
Mottram, J. C., Hoare, M. G., Davies, B., et al. 2011, ApJ, 730, L33
Nguyen Luong, Q., Motte, F., Schuller, F., et al. 2011, A&A, 529, A41
Nguyen-Luong, Q., Motte, F., Carlhoff, P., et al. 2013, ApJ, 775, 88
Nony, T., Galvan-Madrid, R., Motte, F., et al. 2023, A&A, 674, A75
Padoan, P., Pan, L., Juvela, M., Haugbølle, T., & Nordlund, Å. 2020, ApJ, 900, 82
Panagia, N. 1973, AJ, 78, 929
Pillai, T., Kauffmann, J., Wyrowski, F., et al. 2011, A&A, 530, A118
Pouteau, Y., Motte, F., Nony, T., et al. 2023, A&A, 674, A76
Priestley, F. D., & Whitworth, A. P. 2021, MNRAS, 506, 775
Redaelli, E., Bovino, S., Giannetti, A., et al. 2021, A&A, 650, A202
Rosolowsky, E. W., Pineda, J. E., Kauffmann, J., & Goodman, A. A. 2008, ApJ, 679, 1338
Rubin, R. H. 1968, ApJ, 154, 391
Sakre, N., Habe, A., Pettitt, A. R., & Okamoto, T. 2021, PASJ, 73, S385
Schilke, P., Walmsley, C. M., Pineau des Forets, G., & Flower, D. R. 1997, A&A, 321, 293
Sipilä, O., Caselli, P., & Harju, J. 2013, A&A, 554, A92
Sipilä, O., Harju, J., Caselli, P., & Schlemmer, S. 2015, A&A, 581, A122
Sipilä, O., Caselli, P., & Harju, J. 2019a, A&A, 631, A63
Sipilä, O., Caselli, P., Redaelli, E., Juvela, M., & Bizzocchi, L. 2019b, MNRAS, 487, 1269
Snow, T. P., & Witt, A. N. 1996, ApJ, 468, L65
Spitzer, L. 1978, Physical processes in the interstellar medium (New York: Wiley)
Tafalla, M., Myers, P. C., Caselli, P., Walmsley, C. M., & Comito, C. 2002, ApJ, 569, 815
Takahira, K., Tasker, E. J., & Habe, A. 2014, ApJ, 792, 63
Takahira, K., Shima, K., Habe, A., & Tasker, E. J. 2018, PASJ, 70, S58
Towner, A. P. M., Ginsburg, A., Dell'Ova, P., et al. 2024, ApJ, 960, 48
Tremblin, P., Anderson, L. D., Didelon, P., et al. 2014, A&A, 568, A4
Urquhart, J. S., König, C., Giannetti, A., et al. 2018, MNRAS, 473, 1059
van der Tak, F. F. S., Black, J. H., Schöier, F. L., Jansen, D. J., & van Dishoeck, E. F. 2007, A&A, 468, 627
Vázquez-Semadeni, E., Palau, A., Ballesteros-Paredes, J., Gómez, G. C., & Zamora-Avilés, M. 2019, MNRAS, 490, 3061
Whitworth, A. P., Bhattal, A. S., Chapman, S. J., Disney, M. J., & Turner, J. A. 1994a, A&A, 290, 421
Whitworth, A. P., Bhattal, A. S., Chapman, S. J., Disney, M. J., & Turner, J. A. 1994b, MNRAS, 268, 291
Wiesenfeld, L., & Faure, A. 2013, MNRAS, 432, 2573
Wu, B., Tan, J. C., Nakamura, F., et al. 2017, ApJ, 835, 137
Zhang, B., Moscadelli, L., Sato, M., et al. 2014, ApJ, 781, 89
Zhang, C.-P., Li, G.-X., Pillai, T., et al. 2020, A&A, 638, A105
Zinnecker, H., & Yorke, H. W. 2007, ARA&A, 45, 481

Appendix A: Distribution of dense gas: Multiple velocity components

We present in Figure A.1 the integrated intensity maps of molecular lines $H^{13}CO^+$ (1-0), HC_3N (9-8), SiO (2–1), CS (2–1) and H_2CS $3_{1,3}$-$2_{1,2}$, CH_3OH 2(1)-1(1) *A*, CCH $1_{1,1}$-$0_{1,1}$, CH_3CCH (6-5), for the three clumps MM2, MM3, C in the north and two clumps F1, F2 in the south (Fig. 1). For all maps, the velocity ranges for integration are 80-100 km s^{-1}. For the northern and southern region, we selected 5 and 4 representative sub-regions (R1-R5, SR1-SR4), marked as rectangles in Figure A.1 and the average spectra of these regions are shown in Figures A.2 and A.3.

For the northern region encompassing clumps MM2, MM3, and C, the strongest emission of all lines except SiO (2–1) coincides with sub-region R5, the central region of clump MM2, while emission of SiO (2–1) peaks at sub-region R4, the connecting region of clumps MM2 and MM3. With respect to the morphology of the line emission, SiO (2–1) exhibits the most elongated structure along the northeast-southwesterly direction, concentrated in the central region of the primary beam. Comparing the molecular gas distribution to the 3 mm continuum, the source MM2 has peak line emission in good correlation with the continuum emission (sub-region R5), while the source MM3 has a line emission peaking offset (sub-region R3) from the continuum, indicating strong absorption towards the densest UCHII region. In particular, the $H^{13}CO^+$ (1-0) line shows negative absorption dip at 97-101 km s^{-1}.

The southern region composed of F1 and F2 exhibits a less concentrated distribution of line emission, having multiple localised emission peaks. In clump F1, except for the core F1-c2, the filament of the 3 mm continuum appears mostly offset from the line emission peak. Clump F2 shows extended and rather uniform line emission, except SiO (2–1), which shows clumpy structures, as can be seen in sub-region SR4.

The individual integrated intensity maps (channel maps) of the same set of lines are shown in Figures A.4-A.6. The corresponding velocity intervals are chosen according to the line profile of the averaged spectrum of CS (2–1) in the two regions.

For the northern region, there are at least three velocity components peaking in velocity ranges of 80-92 km s^{-1}, 92-96 km s^{-1}, and 96-108 km s^{-1}. Compared to the emission of $H^{13}CO^+$(1-0) and HC_3N (9-8), the emission of CS(2–1) and SiO (2–1) show more extended structures in the 80-92 km s^{-1} (most blue-shifted) velocity range, prominent in the whole northwestern region of the map. In this velocity range, towards clump C, the emission morphology of these two set of lines is also different, with CS(2–1) and SO 2_3-1_2 showing elongated structures roughly along the north-south direction; and the emission of $H^{13}CO^+$(1-0) and HC_3N (9-8) is directed in the northwest-southeast. Clump MM3 hosts many sub-regions of clumpy emission in the south of the 3 mm continuum, which are present in all lines in the velocity range 92-96 km s^{-1} and 96-108 km s^{-1}. Towards clump MM2 in the 92-96 km s^{-1} velocity range, the emission of CS (2–1) line is very weak compared to all the other lines, but appears again in the red-shifted 96-108 km s^{-1} range, which is likely due to strong self-absorption. Comparing the emission morphology of CS (2–1) and SiO (2–1), it seems the emission region of the red-shifted velocity component and the blue-shifted one mostly intersect with each other at clump MM3 and C, and overlap with each other at clump MM2. We discuss this feature further in Sect. 3.3, which points to a cloud-cloud collision process.

The southern region containing clumps F1 and F2 (Figure A.6) has a velocity field of a higher complexity, showing at least five velocity components, in ranges of 76-82, 82-88, 88-93, 93-97.5, and 97.5-103.5 km s^{-1}. Clump F2 has dominant emission separated in two velocity ranges 76-82 km s^{-1} and 88-93 km s^{-1}, and appears rather compact in the $H^{13}CO^+$(1-0) and HC_3N (9-8) emission, while Clump F1 shows emission in four velocity ranges except 76-82 km s^{-1}. The morphology of the line emission of clump F1 is quite complex, which seems to be mainly composed of three parallel filaments in the east-west direction in the velocity range of 88-93 km s^{-1}. Interestingly, from the integrated intensity maps of $H^{13}CO^+$(1-0) and HC_3N (9-8) of the velocity range 93-97.5 km s^{-1}, the filament associated with clump F1 is directed toward the northeast-southwest.

In Figure A.5, we also show the channel maps of H_2CS $3_{1,3}$-$2_{1,2}$, CH_3OH 2(1)-1(1) *A*, CCH $1_{1,1}$-$0_{1,1}$, and CH_3CCH (6-5) K=2 lines of the northern region, which are of same velocity ranges as Figure A.4.

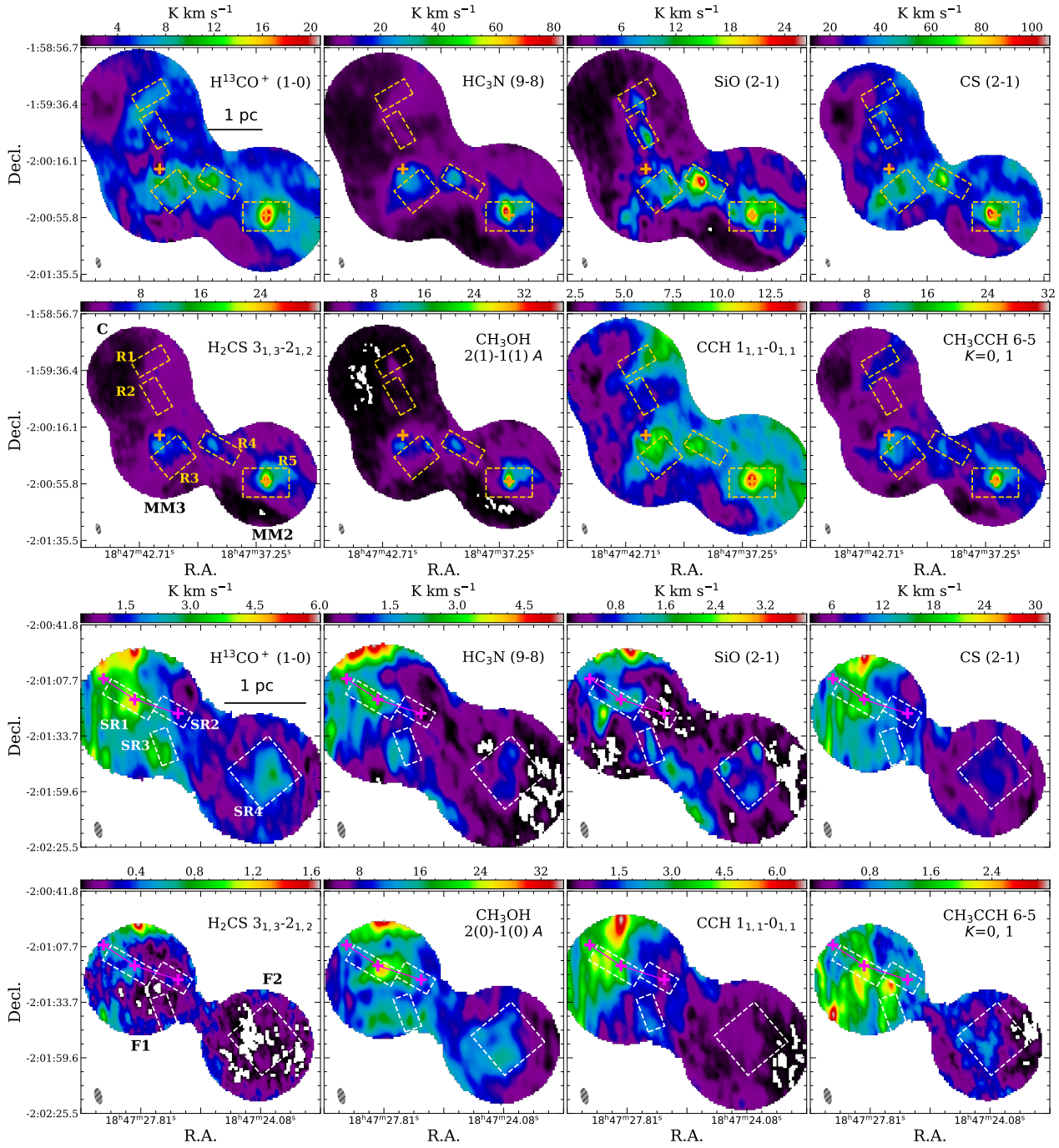

Fig. A.1. Distribution of molecular gas tracers towards the surveyed massive clumps. *Upper panel*: integrated intensity maps of multiple molecular lines towards clumps MM2, MM3 and C. *Lower panel*: Integrated intensity maps of multiple molecular lines towards clump F1 and F2. For both panels, the velocity range for integration for both regions is [80, 100] km s^{-1}. Before generating the integrated intensity maps, all channels with intensity <0.1 K (2σ) are masked.

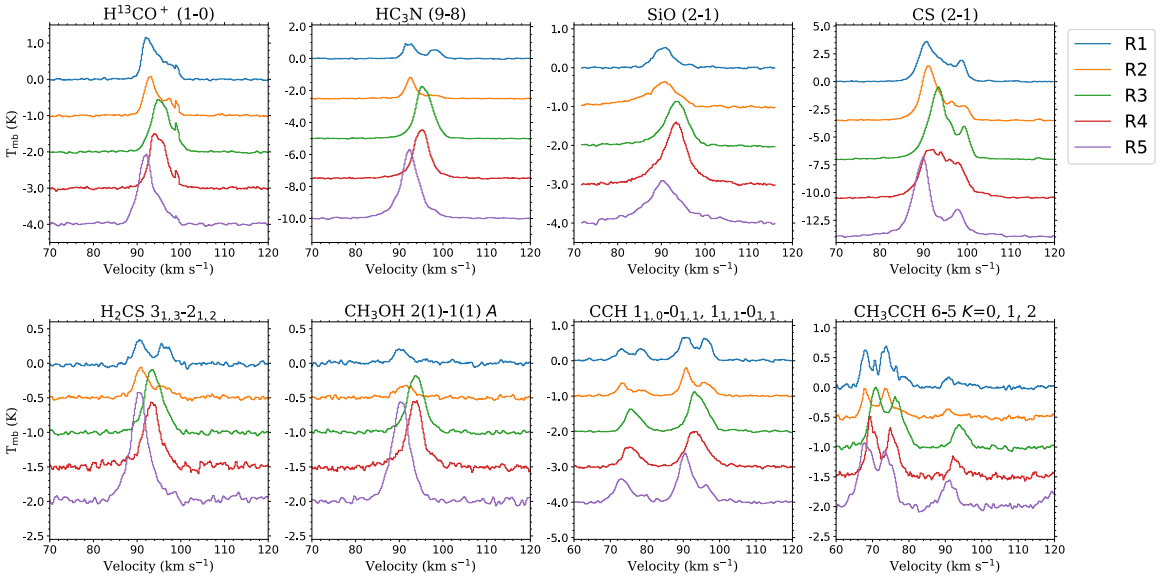

Fig. A.2. Average spectra in sub-regions R1-R5 associated with clumps MM2, MM3, and C. The sub-regions R1-R5 are shown in Fig. A.1.

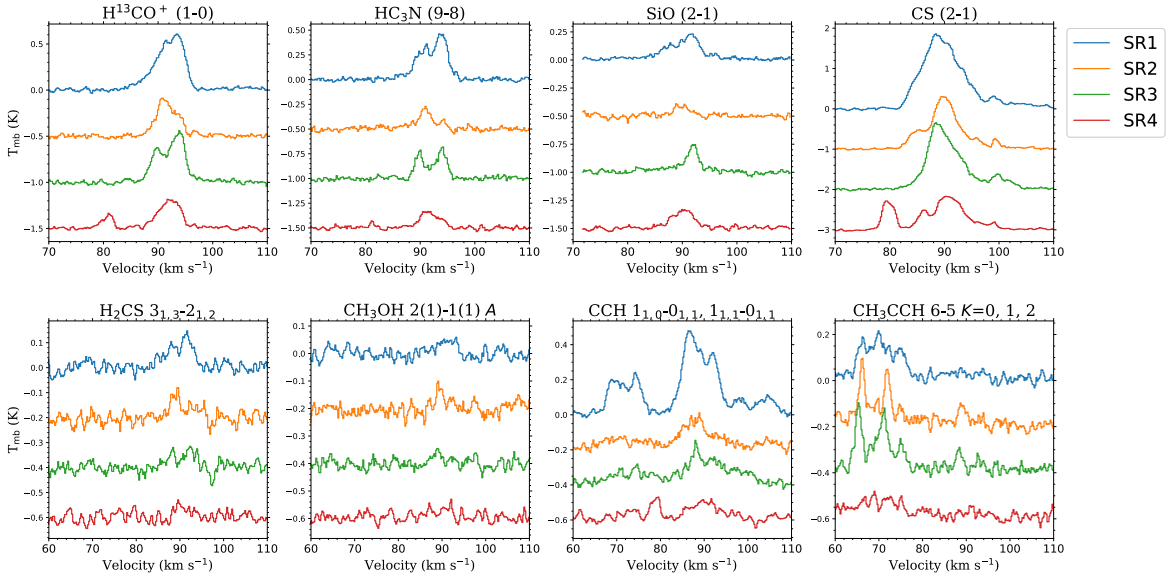

Fig. A.3. Average spectra in sub-regions SR1-SR4 associated with clump F1 and F2. The sub-regions SR1-SR4 are shown in Fig. A.1.

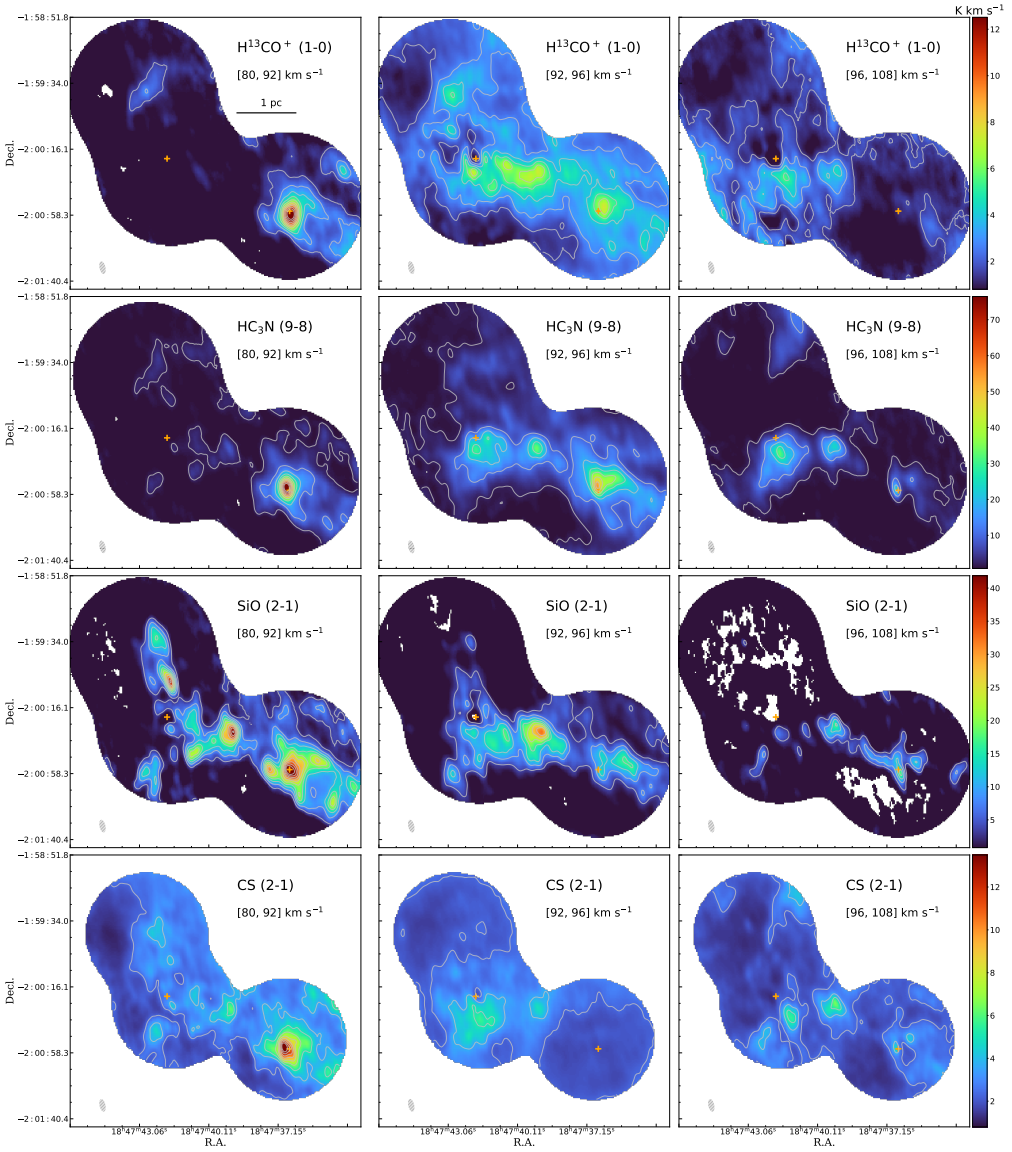

Fig. A.4. Integrated intensity maps of CS (2–1), SO (2_3-1_2), $H^{13}CO^+$ (1-0), and HC_3N (9-8). The velocity ranges for integration are indicated in each subplot, which are selected based on the present velocity components of the overall average spectrum of CS (2–1) line. The 3 mm continuum peaks of clump MM3 and MM2 are indicated as orange crosses. Contour levels start from 1.6 K km s^{-1} to the peak integrated intensities of the [80, 92] km s^{-1} range with eight uniform intervals. The peak integrated intensities are 76.4, 29.0, 12.5, 41.9 K km s^{-1} for CS (2–1), SO (2_3-1_2), $H^{13}CO^+$ (1-0), and HC_3N (9-8), respectively.

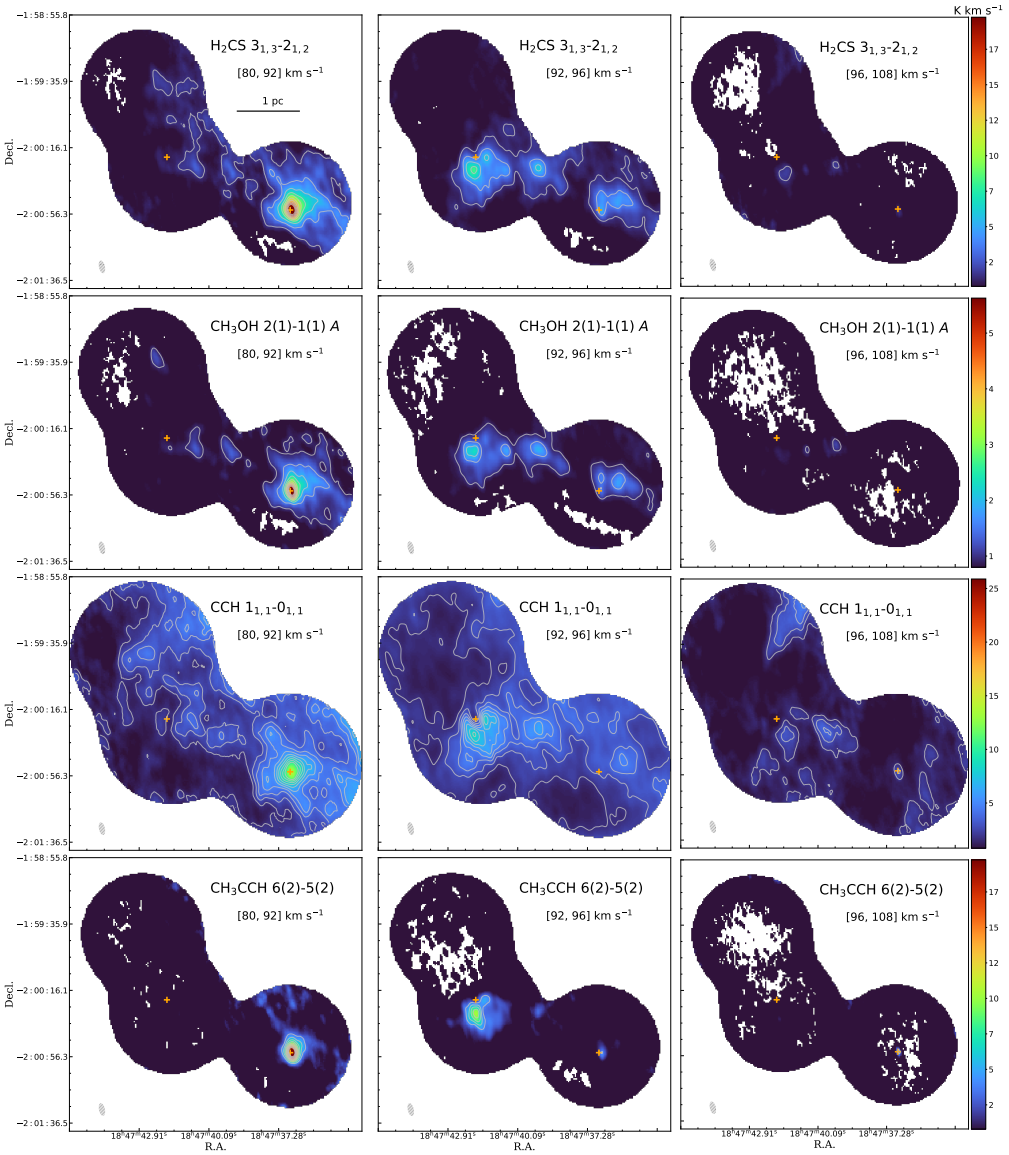

Fig. A.5. Integrated intensity maps of CS (2–1), SO (2_3-1_2), $H^{13}CO^+$ (1-0), and HC_3N (9-8). The velocity ranges for integration are indicated in each subplot, which are selected based on the present velocity components of the overall average spectrum of CS (2–1) line. The 3 mm continuum peaks of clump MM3 and MM2 are indicated as orange crosses. Contour levels start from 1.6 K km s^{-1} to the peak integrated intensities of the [80, 92] km s^{-1} range with eight uniform intervals. The peak integrated intensities are 76.4, 29.0, 12.5, 41.9 K km s^{-1} for CS (2–1), SO (2_3-1_2), $H^{13}CO^+$ (1-0), and HC_3N (9-8), respectively.

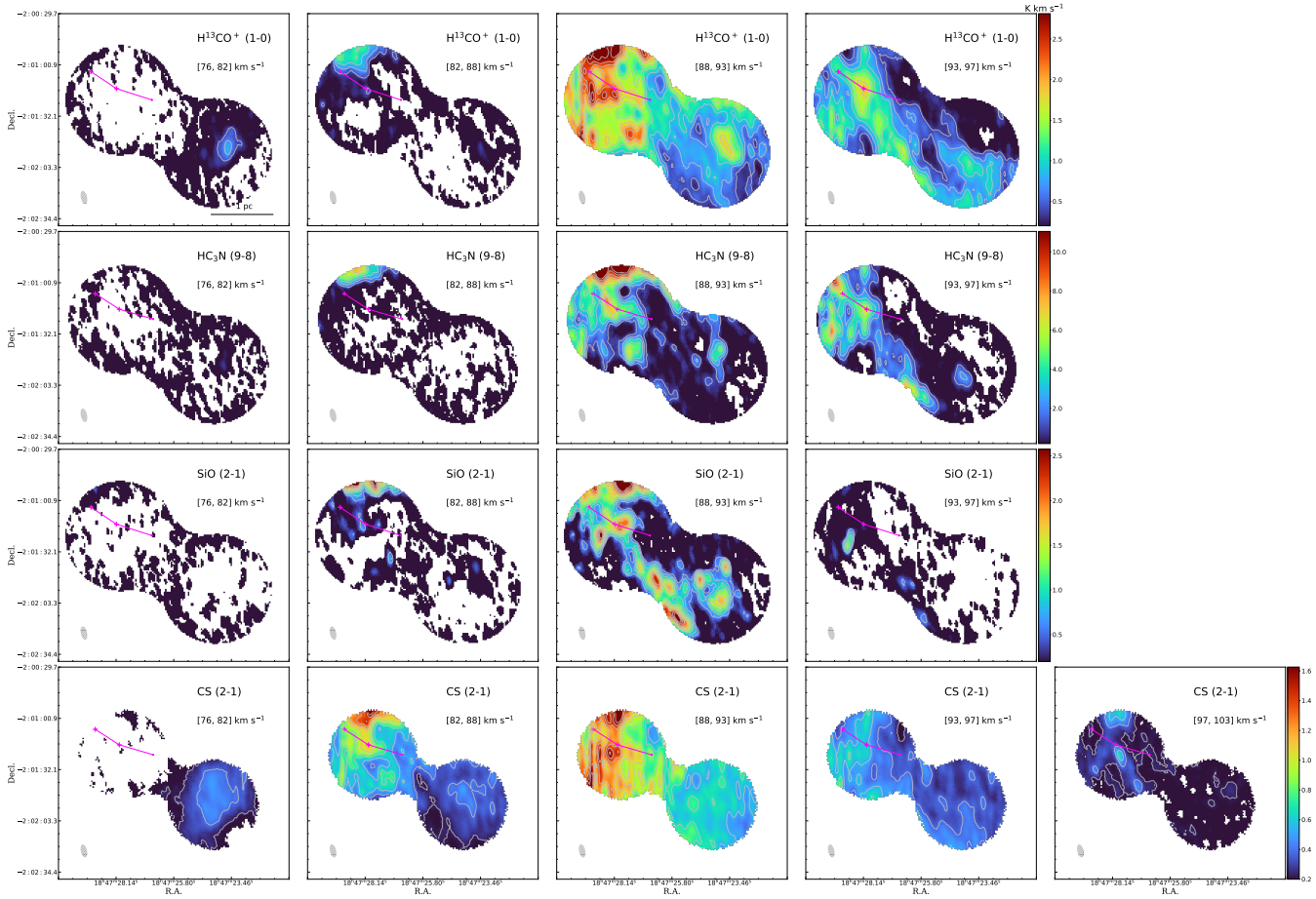

Fig. A.6. Same as Figure A.4, but for the southern region containing clump F1 and F2. The 3 mm continuum peaks of clump F2 are indicated as orange crosses and linked with lines to indicate the filament ridge. Contour levels start from 0.4 K km s^{-1} to the peak integrated intensities of the [88, 93] km s^{-1} range with eight uniform intervals. The peak integrated intensities are 11.3, 4.8, 2.8, 2.6 K km s^{-1} for CS (2–1), SO (2_3-1_2), $H^{13}CO^+$ (1-0), and HC_3N (9-8), respectively. Integrated intensity maps of certain velocity range for some lines are trimmed if the emission is not significant.

Appendix B: Other maps

We present the derived rotational temperature maps from H_2CS (3–2) lines in Fig. B.1. Compared to rotational temperature maps derived by CH_3CCH lines (Fig. 5) the peaking is not as significant and the overall temperature distributions show mostly localised variations without a clear pattern.

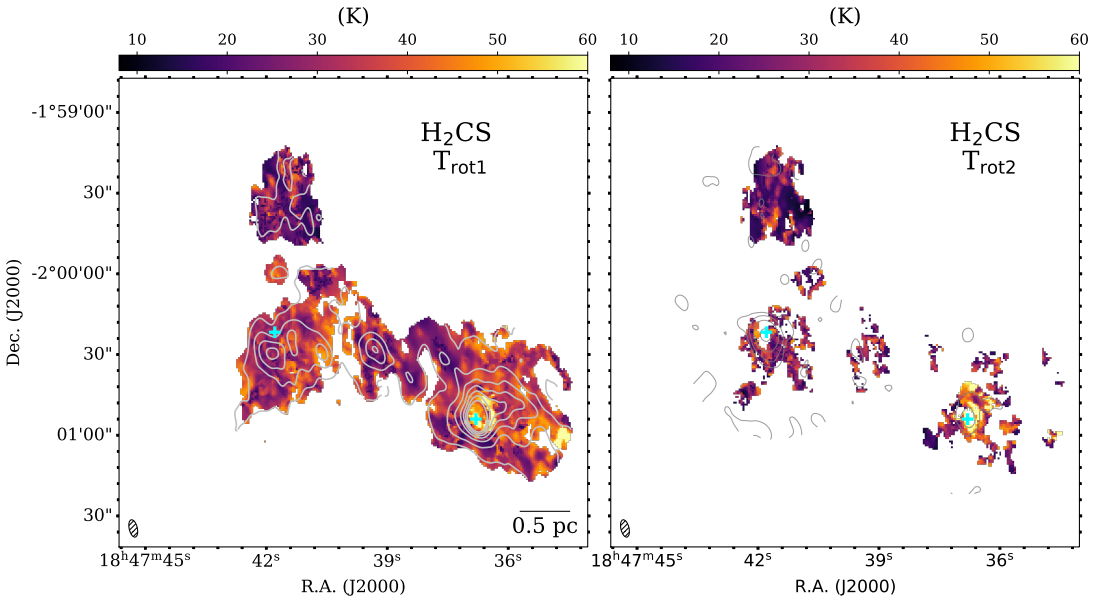

Fig. B.1. Rotational temperature maps derived by H_2CS (3–2) lines for clumps MM2, MM3, and C. The left and right panels show the temperatures from the two component LTE models separately. In the left panel, the contours represent integrated intensity map of H_2CS 3(1,3)-2(1,2) line. The velocity range for integration is 80-100 km s^{-1} and the contour levels are from 2.7 K km s^{-1} (6 σ) to 16.1 K km s^{-1} (0.5 times peak emission value of MM2) with seven uniform intervals. In the right panel, the contours represent the 3 mm continuum emission, and are logrithmic-spaced from $2\sigma_v$ (σ_v = 1.6 mJy beam^{-1}) to 225.0 mJy beam^{-1} with five intervals (same as Figure 2). In both plots, the cyan crosses indicate the position of the peak intensity of 3 mm emission.

Appendix C: Two-component *hfs* fitting results of the CCH line

We present the derived parameter maps from LTE modelling of C_2H (1-0) hyperfine lines in Fig. C.1-C.4.

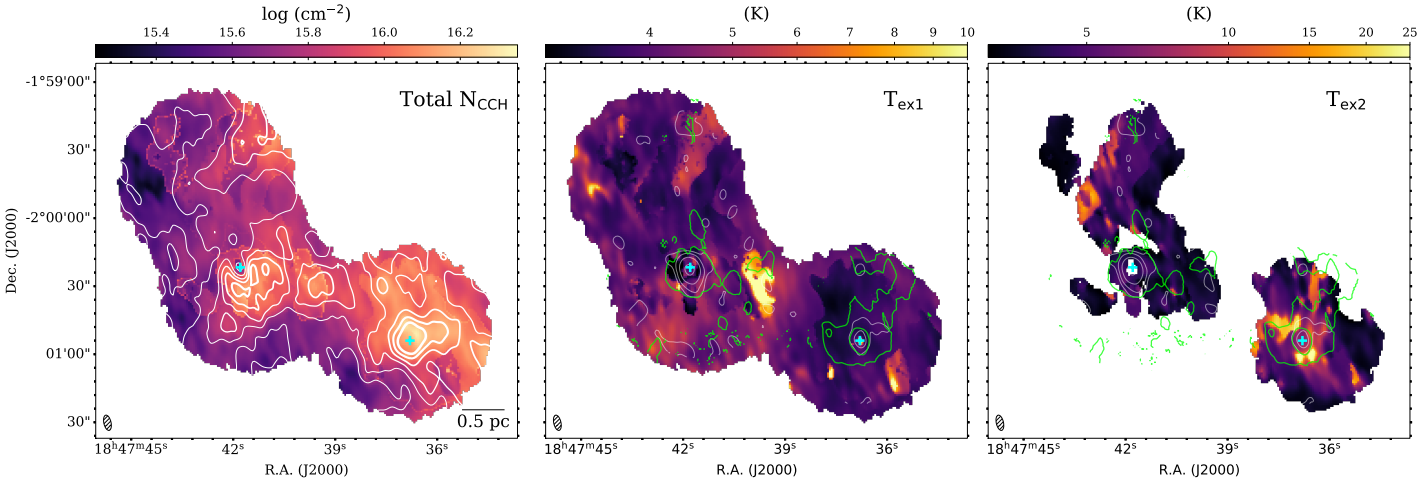

Fig. C.1. CCH column density and excitation temperatures from the two-component *hfs* fitting for clumps MM2, MM3 and C. White contours in the left panels represent the integrated intensity map of CCH $1_{1,1}$-$0_{1,1}$ line (85-100 km s^{-1}), from 3.3 K km s^{-1} (7 σ) to 9.8 K km s^{-1} (0.9 times the peak emission of MM2) with six uniform intervals. The gray and green contours and crosses follow the same definitions as in Figure B.1.

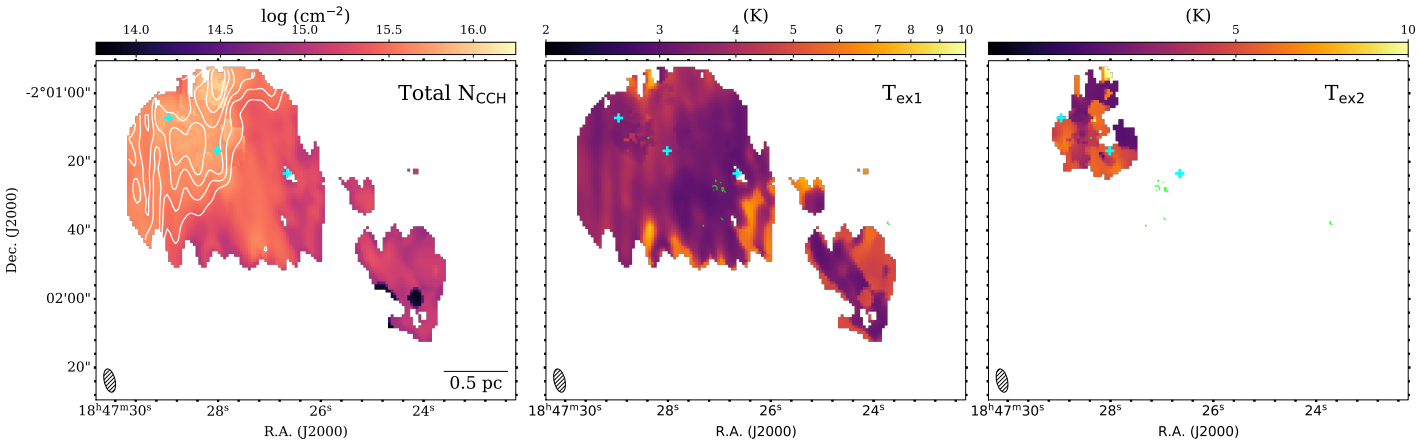

Fig. C.2. Same as Figure C.1, but for clump F1 and F2. White contours in the left panels represent the integrated intensity map of CCH $1_{1,1}$-$0_{1,1}$ line (80-95 km s^{-1}), from 2.2 K km s^{-1} (7 σ) to 6.0 K km s^{-1} (0.9 times the peak emission of F1) with six uniform intervals.

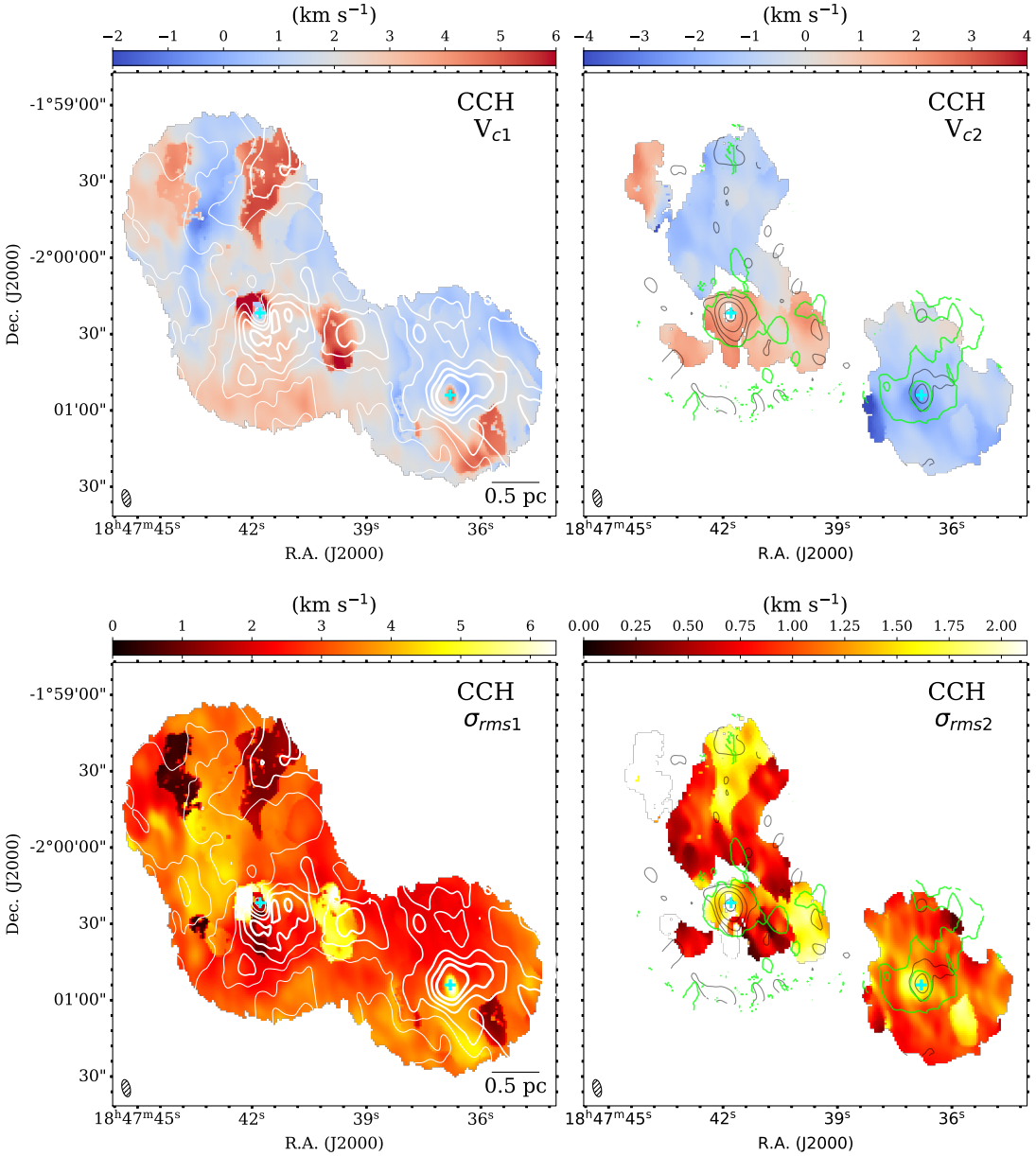

Fig. C.3. Centroid velocity and velocity dispersion distribution of the two-component Gaussian fits of CCH (1-0) *hfs* lines (ν~87.3 GHz) for clumps MM2, MM3, and C. The upper and lower panels show the two components individually. White contours in left panels follow same definitions as in Figure C.1, representing the integrated intensity map of CCH. In both the upper and lower panels, the gray and green contours and crosses in left and right plot follow the same definitions as in Figure B.1.

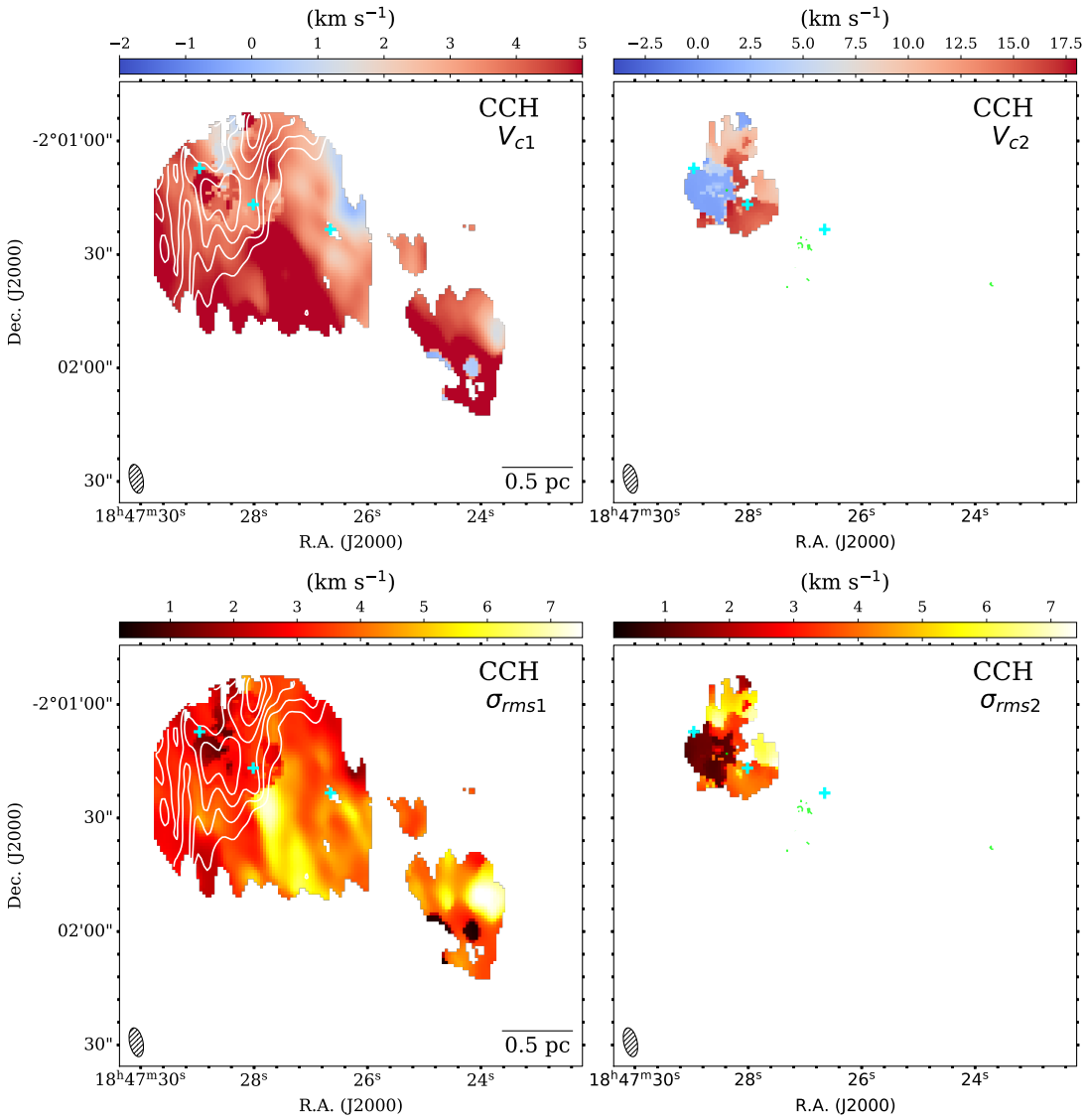

Fig. C.4. Same as Figure C.3, but for the clumps F1 and F2. White contours in left panels follow same definitions as in Figure C.2, representing the integrated intensity map of CCH.

Appendix D: NH_2D spectra of the identified cores

We plot the core averaged NH_2D spectra and the fitted spectra in Fig. D.1 and D.2. In Fig. D.3, an example of posterior distribution of parameters of the two-component fit is shown.

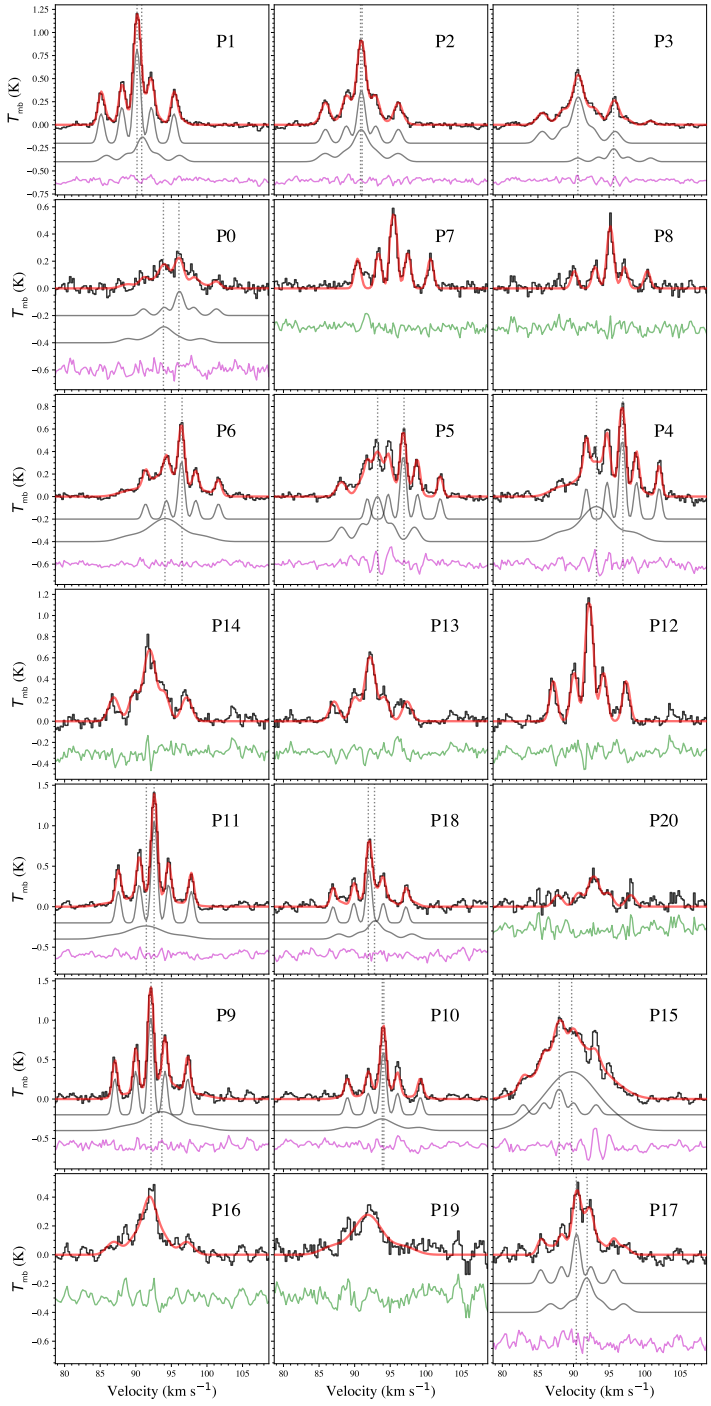

Fig. D.1. NH_2D spectra of the `dendrogram` identified cores in clumps MM2, MM3, and C. For cores that a single *hfs* component fit suffices to reproduce the line profile, the model is shown as red line, whereas two-component *hfs* fits are shown as blue (sum) line and gray lines (manually adding offset from zero level) for the two components, separately. Vertical dotted lines indicate the peak velocity of the two-component models. The core names are denoted as Pn with n of integers between [0, 20] (Fig. 14, upper panels). The subplots are arranged such that the corresponding cores are located from north-east to south-west along the mosaic region.

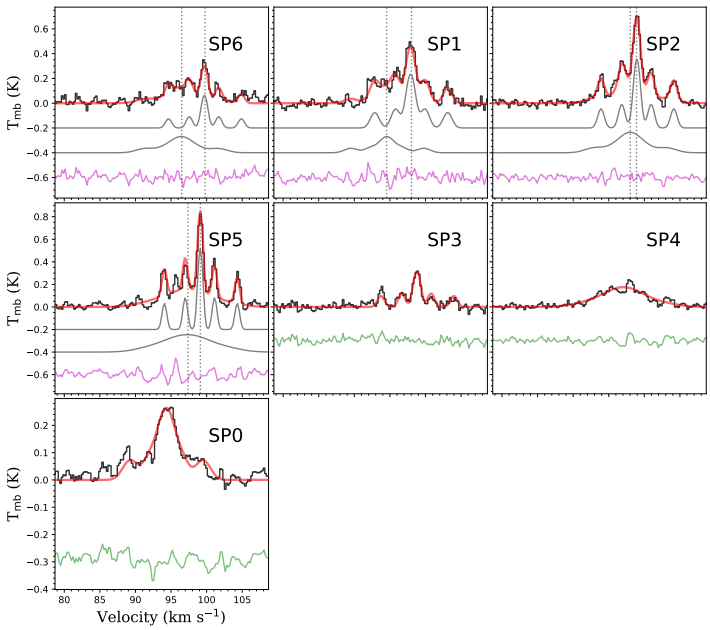

Fig. D.2. Same as Figure D.1, but for NH_2D spectra of cores residing in clumps F1 and F2. The core names are denoted as SPn with n of integers between [0, 6] (Figure. 14, lower panels).

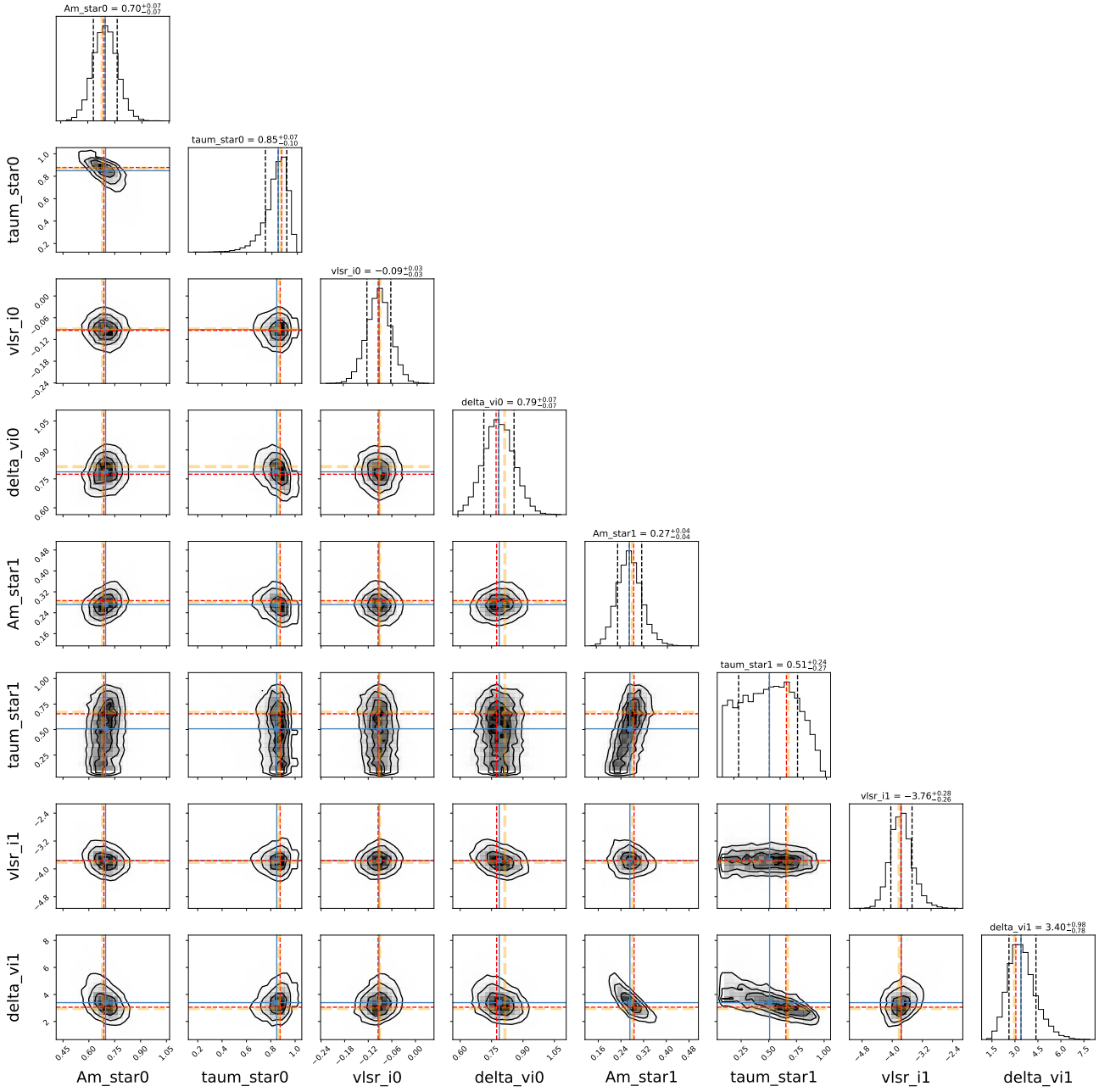

Fig. D.3. Posterior distribution of the parameters from two-component *hfs* fitting of core P4. Black vertical dotted lines indicate the 1σ quantiles of the distribution. The other coloured vertical lines indicate the parameter set corresponding to the least-square fit (red), the median (blue) and maximum-likelihood (orange) values drawn from the posterior distribution.